END
DATE
FILMED

DTIC

LEVEL II ②

NAVAL POSTGRADUATE SCHOOL
Monterey, California

DTIC
ELECTE
DEC 0 4 1980

E

STUDY OF GAS DYNAMIC EFFECTS IN NON-UNIFORM
HIGH PRESSURE ELECTRICAL DISCHARGES

Jon L. Barto

August 1980

Approved for public release; distribution unlimited.

Prepared for: Chief of Naval Research
Arlington, VA 22217

80 12 01 245

NAVAL POSTGRADUATE SCHOOL

Monterey, California

Rear Admiral J. J. Ekelund   D. A. Schrady
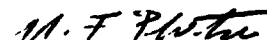Superintendent   Acting Provost

This report was prepared by:

J. L. BARTO

Reviewed by: Released by:

M. F. PLATZER, CHAIRMAN   W. M. TOLLES
DEPARTMENT OF AERONAUTICS   DEAN OF RESEARCH

(16) RR00004

REPORT DOCUMENTATION PAGE		READ INSTRUCTIONS BEFORE COMPLETING FORM
1. REPORT NUMBER 14 NPS67-80-005	2. GOVT ACCESSION NO. AD-A092413	3. RECIPIENT'S CATALOG NUMBER (9) Rept. for
4. TITLE (and Subtitle) (6) STUDY OF GAS DYNAMIC EFFECTS IN NON-UNIFORM HIGH PRESSURE ELECTRICAL DISCHARGES.		5. TYPE OF REPORT & PERIOD COVERED 27 May — 2 Aug 1980 6. PERFORMING ORG. REPORT NUMBER
7. AUTHOR(s) Jon L. Barto		8. CONTRACT OR GRANT NUMBER(s) (17)
9. PERFORMING ORGANIZATION NAME AND ADDRESS NAVAL POSTGRADUATE SCHOOL MONTEREY, CA 93940		10. PROGRAM ELEMENT, PROJECT, TASK AREA & WORK UNIT NUMBERS 61152N RR000 01 10 N0001480WR00054
11. CONTROLLING OFFICE NAME AND ADDRESS NAVAL POSTGRADUATE SCHOOL MONTEREY, CA 93940		12. REPORT DATE Aug 1980 13. NUMBER OF PAGES 79
14. MONITORING AGENCY NAME & ADDRESS(If different from Controlling Office) NAVAL POSTGRADUATE SCHOOL MONTEREY, CA 93940 (12) 89		15. SECURITY CLASS. (of this report) UNCLASSIFIED 15a. DECLASSIFICATION/DOWNGRADING SCHEDULE

16. DISTRIBUTION STATEMENT (of this Report)

Approved for public release, distribution unlimited.

17. DISTRIBUTION STATEMENT (of the abstract entered in Block 20, if different from Report)

18. SUPPLEMENTARY NOTES

19. KEY WORDS (Continue on reverse side if necessary and identify by block number)

electrical discharges, electrode geometries, non-uniform, high pressure discharge model, gas dynamics, electrical lasers, anode extension model.

20. ABSTRACT (Continue on reverse side if necessary and identify by block number) This report examines gas dynamic stabilization of high pressure, highly non-uniform electrical discharges for two electrode geometries. The geometries studied are the multiple-point to plane and the multiple-wire to plane. A successful analytical model is developed utilizing the anode extension concept, which describes the interactions and stabilizing effects of flow, separating the effects of convection and turbulence, in the point-plane geometry. Comparisons of theory and data are presented, illustrating actual observed and calculated breakdown voltages and currents for a number of cases. Flow stabilized high power density electric discharges are

DD FORM 1473 EDITION OF 1 NOV 65 IS OBSOLETE
1 JAN 73
S/N 0102-014-6601

i

applicable to high power electric discharge lasers, magnetohydrodynamic power generation, and other new systems and technologies.

TABLE OF CONTENTS

iii

LIST OF FIGURES

LIST OF SYMBOLS

<u>SYMBOL</u>

A	Stoletow gas constant
B	Stoletow gas constant
C	Proportionality constant
c	Proportionality constant
d	Gap length
d'	Effective gap length
E	Electric field strength
e	Electronic charge (1.601×10^{-19} coulombs)
e	Exponential function (2.718...)
$f(\delta)$	Function of δ
I, i	Total current
j	Local current density
K	Dimensional constant
k	Charged particle mobility
L_x	Length of anode extension (same as δ)
M	Coefficient describing conductor surface (0.6-1.0)
m	Variable exponent of convective term
N	Neutral gas particle density
n	Local species number density
	- Also variable exponent of $\delta*$ term
P	Pressure
ΔP	Maximum local pressure fluctuation due to turbulence
R	Point/wire electrode radius
r	Avalanche radius

S	Slip parameter (u/v_d)
T	Temperature
t_{REC}	Characteristic recombination time
$\bar{U}$, u	Gas flow velocity
$\sqrt{\overline{u'^2}}$	Fluctuating velocity component in turbulent flow
V	applied voltage
$v_{i,e}$	Particle velocities
x	Axial distance measurement
x_c	Axial distance into gap at which $E = E_i$ for non-uniform electrode geometry
x_d	Charged particle drift distance during its lifetime
α	Townsend first ionization coefficient
γ	Second ionization coefficient (electron flow rate)
δ	Anode extension axial dimension
Δ	Function of pressure and temperature
ξ	Turbulence intensity coefficient
ρ	Recombination coefficient
∞	Infinity

COMMON SUPER/SUB-SCRIPTS

SUPERSCRIPTS

*	Flow variable normalized by no-flow value
+,-	Positive or negative charged particle property

SUBSCRIPTS

b	Value at breakdown
c	Value at corona initiation
d	Drift value

e	Electron property
i	Ion property
o	No-flow value
p	Value at point surface
u	Value in a flow field
w	Value at wire surface

ABSTRACT

This report examines gas dynamic stabilization of high pressure, highly non-uniform electrical discharges for two electrode geometries. The geometries studied are the multiple-point to plane and the multiple-wire to plane. A successful analytical model is developed utilizing the anode extension concept, which describes the interactions and stabilizing effects of flow, separating the effects of convection and turbulence, in the point-plane geometry. Comparisons of theory and data are presented, illustrating actual observed and calculated breakdown voltages and currents for a number of cases. Flow stabilized high power density electric discharges are applicable to high power electric discharge lasers, magnetohydrodynamic power generation, and other new systems and technologies.

I. INTRODUCTION

A. Background

Electric discharges have been the subject of intensive study for many years. Numerous books, papers, reports, etc. have been published which characterize and analyse the various complex and interrelated processes which take place in discharges of several gas compositions, pressures, and electrode geometries. The primary objective in most of these studies has been to attempt to relate the atomic level processes to the observed macroscopic discharge properties such as breakdown voltage, current and overall discharge stability for use in engineering analysis and application in design. Some of the more established applications of this type of gaseous electronics include glow discharge lighting, the high voltage arc, corona discharge analysis around power lines and power line design, high voltage switching, spark plug and spark gap design, thermal printing devices and many others.

More recent applications of this electric discharge technology have been generally aimed at systems which are geared to creating very high power densities within the discharge, thrusting physicists and engineers headlong into a direct confrontation with the stability problem, not just with the idea of "defining the envelope", to use an aeronautical term, but to develop ways of expanding the natural discharge stability boundaries through any practical means. The recent high power applications of which we speak include magnetohydrodynamic (MHD) power generation, plasma chemistry, electric discharge convection lasers, E-beam ionizer-sustainer lasers and others.

1

As a result of this growing requirement for increasingly higher power densities, many analyses have been done in the stability area and much insight has been gained in the many modes and regimes from which discharge instability can develop to cause a severe local breakdown in a delicate balance of parameters. One of the successful techniques which has appeared in the engineering of high power density systems is the pulsed system where-in the pulse time is shorter than the characteristic times of the various instability modes which must be avoided. The E-beam and pulsed ionizer-sustainer lasers are examples of the success of this approach (Reference 1). However, present E-beam systems are large, expensive and delicate. In addition, in order to achieve high average power output from the pulsed systems, while the systems can be scaled up in size to any practical limit, once the size limit has been reached, the only other alternative is to increase the pulse repetition frequency (PRF). But this option is also limited, usually by a characteristic optical cavity clearing time which depends on cycling out by flow the products of one pulse before initiating the next one. Failure to allow sufficient clearing time will result in cumulative space charge and gas heating instabilities with resultant low power breakdown.

Due to the inherent limitations cited above and the implicit dependence of those systems on gasdynamics, the present research has been pursued in order to better define the role of turbulence in a high pressure discharge as has been observed by many researchers (References 2, 3, 4, 5 and 6). An understanding of the fundamental modes of gasdynamic coupling which have been observed to affect breakdown voltage and current may lead

2

to new ways to improve present high power density systems through bulk or electrode boundary layer stabilization techniques; and may also point the way for development of sufficiently high power self-sustained CW electric discharge systems which are inherently more compact, rugged, and less expensive than the types mentioned above.

B.   Present Work

Section A of Part II (Fundamentals of Gasdynamic Effects on a Highly Non-Uniform Electrical Discharge) of this report develops in detail a theoretical model for the calculation of breakdown voltage of a ·i-point to plane (points positive) electric discharge based on the "anode extension" concept initially proposed in Reference 7 and further discussed in Reference 3. The model incorporates flow and turbulence effects and is similar in physical basis to the "corona cloud" model of Hepworth, Klene, and Tozer discussed in Reference 8 for a static (non-flowing) non-uniform electric discharge. The present model successfully separates the gasdynamics into the pure convective and pure turbulence effects, and isolates specific electrode geometry and gas parameters in individual terms. This facilitates understanding of the fundamental relationships between the gas properties, electrode orientation and geometry, and the individual gasdynamic coupling mechanisms.

This section also presents a qualitative discussion of the breakdown characteristics of the uniform and non-uniform discharge geometries highlighting the similarities in a qualitative and semi-quantitative manner. It is shown that Meek's breakdown criterion for the non-flowing, uniform field and the equation developed in Section A for the non-uniform, flowing discharge transform into very nearly identical expressions in the middle ground of a flowing uniform field. This illustrates the general nature of

3

the equations of Section A and provides straightforward physical insight
into the final breakdown mechanisms in the geometric extremes. Radial
diffusion and spreading is considered as related to the mean or "drift"
field in a highly non-uniform geometry.

Section B of the report discusses the typical discharge section used
in Section A with the three rows of pins replaced by three thin wires (see
Fig. 1b). A preliminary analysis which was done in the terms of Reference
9 basically indicated the potential for improving discharge input power by
a factor of 2-3 with the wire anode. Various degrees of discharge input
power enhancement have been noted in similar configuration modifications
in connection with MHD laser/power generation applications (Reference 10).

Recent experimental results in this area are presented and discussed
in relation to the points-plane configuration. To date due to power
supply limitations no improvement in performance has been noted, and some
recommendations for further research in this area are presented, when a
larger power supply is available.

Section C of Part II discusses electrode design geometry and electric
field distributions for optimum electron production and for best reduced
electric field strength (E/N or E/P) for laser pumping.

Part III presents a data summary of current and past point-plane and
wire-plane laboratory work, reviews the theory and experimental trends,
indicating important correlations and features of the anode extension model.

II. FUNDAMENTALS OF GAS DYNAMIC EFFECTS ON A HIGHLY NON-UNIFORM ELECTRICAL DISCHARGE

A.   Prediction of Flow and Turbulence Effects on Breakdown Voltage

   1.   Description of Discharge Geometry for Analytical Formulation

   A significant body of breakdown data has been generated in various highly non-uniform electric field geometries with positive and negative polarities at the highly stressed electrode. The point-to-plane geometry with the points positive, however, has been the particular case through which the present analytical model has been developed; but the model is sufficiently general that the basic flow and electric field interactions described should also be useful in analysis, interpretation, and trouble shooting of many other non-uniform geometries and systems both with and without flow.

   The specific apparatus used in the current research, described in detail in Reference 11 consists of multi-point to plane electrode arrangement (see Fig. 1a) which is mounted in a wind tunnel with available test section velocities on the order of 200 m/s of ambient pressure air. Varying degrees of turbulence can be introduced by placing turbulence generating screens upstream of the electrode set-up. Two flow modes are discussed in this report, namely,

   a.   Normal Flow - directed through the turbulence screen, past the positive multi-pin anode, through the interelectrode gap, and thence through the grounded cathode, which is designed to approximate a plane with low blockage to permit maximum gas flow rates (see Fig. 2a).

   b.   Reverse Flow - same as above except that the anode and cathode positions are reversed (see Fig. 2b) and the turbulence screen was omitted.

5

While our earlier effort which included cross-flow tests (Fig. 2c) was based on an assortment of turbulence screens which produced a variety of spectra and intensities, the present work (which includes verification of past trends, and additional data taking for better curve definition at low speeds) is done utilizing only screen #9 design. This screen proved to be most successful in the prior work (References 3, 7, 11).

2. <u>General Description of the Discharge</u>

With no voltage applied across the gap, and no gas flow, there exist a small number of random electrons present in the gap which are produced by outside sources (Reference 12). As voltage is applied these electrons under the influence of the resultant electric field begin to move toward the anode producing a small saturation current whose magnitude is limited by the number of electrons present and their average drift velocity in the field. In a highly asymmetric geometry such as the point-to-plane, the electric field produced is very non-uniform, being highest at the point surface and falling off rapidly in a hyperbolic fashion with distance from the point as illustrated by the axial field distribution in a hyperboloidal point-to-plane gap (Reference 17) which is assumed in the following analysis:

$$E(x) = \frac{R}{R+x} E_p \tag{1}$$

$R \equiv$ point radius

$x \equiv$ axial distance from point

$E_p \equiv$ field strength at point $\equiv \dfrac{2V}{R\log(4d/R)}$

6

$$V \equiv \text{applied voltage}$$

$$d \equiv \text{gap length}$$

Due to this field asymmetry, as the voltage increases further, the field strength at the point soon reaches a value which permits the free electrons moving toward the point to gain enough energy to ionize by collision some of the gas atoms and molecules near the point surface, thus additional electrons and positive ions are produced resulting in a rise in the current. The voltage at which these first few ionization events occur is called the corona initiation voltage and is usually designated V_c, i.e., when $Ep \approx E_c$, $V \approx V_c$:

$$Ep \to E_c \approx \frac{2V_c}{R\log(4d/R)} \tag{2}$$

$$V_c \approx \frac{E_c R\log(4d/R)}{2} \tag{3}$$

From Reference 13 the threshold field E_c can be calculated from Peek's Law (1929) modified by Gary et al (1972) for a point-to-plane type geometry, i.e.,

$$E_c = E_o M\Delta \left[1 + \frac{K}{(\Delta\frac{R}{2})^{\frac{1}{2}}} \right] \qquad \text{where} \tag{4}$$

$E_o = 31$ KV/cm (near spark breakdown of air)

$M \equiv$ coefficient describing conductor surface (0.6-1.0)

$K \equiv 0.308$ cm$^{\frac{1}{2}}$

$R \equiv$ radius of point

$\Delta \equiv 0.392\, P/(273+T) \equiv 1$ for air at STP

7

$P \equiv$ pressure in torr

$T \equiv$ temperature in $^{\circ}C$

Continued increases in voltage moves the high field region further and further into the gap. At the position where the reduced field value (E/P) is approximately equal to that required for ionization by electron collision (E_i/P), free electrons will begin to produce avalanches into the positive point. From this critical distance x_c, each avalanche will produce an exponential increase in electrons and positive ions left in the aftermath. The number of electrons produced in the non-uniform field is given by the well known expression (Reference 12)

$$n = n_o e^{\int_{x_1}^{x_2} \alpha dx} \tag{5}$$

where

$n_o \equiv$ original number of electrons

$\alpha \equiv$ Townsend's first ionization coefficient

$x \equiv$ avalanche travel distance

The coefficient α is a strong function of the electric field as illustrated by the usual semi-analytical expression found in many references -

$$\alpha = APe^{\frac{BP}{E(x)}} \tag{6}$$

where A and B are gas constants, P is pressure. It is necessary, therefore, to integrate the exponent since in the region under

discussion E and therefore α vary greatly with x as the avalanche rushes toward the point, Fig. 3. An average or effective ionization coefficient can be defined as follows:

$$\bar{\alpha} = \frac{1}{x-x_0} \int_{x_0}^{x} \alpha \; dx \tag{7}$$

which will produce the same number of particles in traveling the same distance, and then we can write

$$n = n_0 e^{\bar{\alpha}(x-x_0)}$$

similar to the simpler uniform field case. In the following discussion the bar will be dropped for convenience, and x_0 assumed to be 0. Due to the much greater electron drift velocities, the electrons from these avalanches are quickly drawn into the positive point leaving the positive ions behind in a maelstrom of activity including electrostatic repulsion from the positive point, diffusion in all directions, neutralization by recombination with other electrons or charge transfer from negative ions, etc. All of these processes tend to dissipate the space charge concentrations and smooth the non-uniformity of the electric field which is generated by the dense space charge near the point, and by the point itself.

However, if the applied voltage is raised high enough (near breakdown), these dissipative processes lag behind production processes,

9

and the space charge density and field intensity can become of the same order of magnitude as the applied field. When this happens, the portion of the gap external to the high field region is no longer able to distinguish the applied field nor the position of the point, and the dense space charge actually assumes the role of the point forming a "virtual" anode (Reference 14) effectively diminishing the gap as seen from the cathode. The effect of this "extension" of the point is to require dissipation of the applied voltage over a shorter gap, thus raising the "drift" (low field) portion of the gap to a uniformly higher level (Fig. 4). Reference 14 illustrates how, in a non-uniform geometry, the presence of space charge can modify an originally hyperbolic field distribution to produce a uniform field over most of the gap in concentric cylinders where the inner electrode radius is much less than the outer.

Another important effect which must be accounted for is the radial diffusion of the space charge in the ionization region which essentially distorts the shape of the original point, making the resultant virtual anode appear extended in the radial as well as the axial dimension (see Fig. 5).

It will be seen in the following analysis, that accounting for the two effects (shortened gap, and modified radius) provides much insight into various discharge phenomena heretofore not well explained and leads to a very general form of the breakdown equation for a highly non-uniform geometry in a turbulent flow field. The breakdown equation is derived by accounting for modifications by the flow of the quasi-static space charge distributions which develop in the non-flowing running discharge case. The trends revealed and results obtained are

10

fundamental and adaptable to different gas mixtures, geometries, and flow field parameters.

3. Analytical Development of the Breakdown Equation with Flow Interactions

The exponential charged particle multiplication process in high reduced fields has already been mentioned. Since the current is produced by the motion of these particles between the electrodes, the current density can be written as a summation of the individual species contributions. For the present it is assumed that the positive ion and electron currents dominate the discharge (Reference 8). The current density will then be given by

$$j = j_i - j_e = en_i v_i + en_e v_e \qquad (8)$$

where

$j \equiv$ local current density

$e \equiv$ electronic charge (1.6×10^{-19} coulombs)

$v_{i,e} \equiv$ ion/electron drift velocities

$n_{i,e} \equiv$ local charge densities

Considering only the high field ionization region, if each electron entering causes an electron avalanche, the average number of electrons produced is equal to the multiplication factor plus one, while the number of positive ions produced would be just the multiplication factor. The multiplication factor is usually so high, that the number of positive ions and electrons created in this region are identical. Therefore

11

$$n_i \approx n_e \approx n \qquad\qquad (9)$$

Due to the relatively low mobility of the positive ions, the majority of electrons continue into the anode and a region of growing positive space charge is produced in the immediate vicinity which will slowly begin to drift away due to electrostatic repulsion from the anode. Under these conditions the current density can be estimated by the following

$$j = en\ (v_i + v_e) \qquad\qquad (10)$$

Under conditions of low positive space charge, v_e is much greater than v_i and the equation reduces to

$$j \approx env_e$$

But if the positive space charge field becomes of the same order of magnitude as the local applied field, electrons may be retarded or even trapped by the space charge cloud. In this case the electron drift velocities may be reduced to the same order of magnitude as the ion velocities, or to zero and even negative if the electron is trapped and dragged in the opposite direction by high positive ion fields. In this case, the current density approaches

$$j \approx env_i \qquad\qquad (11)$$

and the particle density may then vary between

12

$$n \approx \frac{j}{ev_e} \quad \text{to} \quad n \approx \frac{j}{ev_i} \qquad (11)$$

It is now proper to return to the "anode extension" concept introduced above. As indicated, when the space charge field near the anode approaches the same order of magnitude as the applied field, flux lines from charges within the remainder of the gap and from the cathode will no longer be able to reach the actual point, but will instead terminate on charges in front of the point. This essentially shortens the gap and to a first approximation, results in dissipation of the applied potential over a reduced distance, raising the mean electric field over the remainder of the gap (Fig. 5).

In order to continue the development, an estimate of the length of the anode extension region (hereafter designated by a δ) is required. A reasonable estimate of the beginning of the region of dense positive charge would be the point at which the applied electric field approaches the breakdown value for the type of gas mixture involved. In our example of atmospheric air, it is assumed that the anode extension in a non-flowing discharge begins at the value $E(x) = 25,000$ volts/cm ($E/P \approx 35$). This assures that the majority of electrons approaching this position avalanche toward the positive point, depositing the slower moving positive ions to form the anode extension (see Fig. 5).

As soon as a space charge concentration develops, however, there are numerous forces and processes which act on and within it to dissipate it. Among the important process to be considered are:

(a) diffusion in all directions,

13

(b) electrostatic repulsion by the electrode of like sign, in
this case the nearby point,

(c) attraction by the opposite electrode which may be
insignificant in this region in very non-uniform fields,

(d) recombination with supplementary electrons supplied from
various sources, i.e., photoelectrons, cathode emission,
free electrons, detachment from negative ions, etc.

In a "running" discharge, i.e., one which has reached a pseudo-steady
mode of operation, a quasi-equilibrium condition is ultimately reached
in which the charge production and dissipation mechanisms locally balance
each other. The result of this balance is a quasi-steady anode extension
with a finite and calculable extent; a distorted radial dimension of the
virtual anode due to radial diffusion, and an increased mean electric
field in the drift region of the discharge (see Fig. 5). Reference 3
alluded to these two important dimensional changes.

To calculate the equilibrium boundary of δ in the axial
dimension between anode and cathode, electrostatic repulsion, convection
(in the flowing case) and recombination must be balanced, diffusion being
small in the high field region compared to the axial component of ion
drift. The radial boundary is determined by radial diffusion, and re-
combination, and in the case of crowded multi-pin electrodes, by symmetry
considerations.

a. The Anode Extension - Axial Dimension - δ

Since the length of δ is determined primarily by a balance
between the ion drift out of the dense space charge region, and the dis-
sipation of that charge by recombination, an expression for recombination

14

is required. The form assumed here as in Reference 3 is the three-body solution of Hinnov and Hirschberg, namely that the recombination time

$$t_{REC} = \frac{1}{2\rho n^2} \qquad (12)$$

where

$\rho \equiv$ recombination coefficient

$n \equiv$ particle density

$t_{REC} \equiv$ characteristic recombination time

Now, the positive space charge created in the vicinity of the anode will be subject to electrostatic repulsion until *it recombines with an electron.* Therefore, the travel distance of an individual ion during its lifetime will be

$$x_d \approx v_i \, t_{REC} \qquad (13)$$

where $v_i \equiv k_i E \equiv$ ion drift velocity. Inside this drift distance will be *much positive space charge,* and outside it, most of the charge will have been neutralized by recombination. Therefore, since

$$x_d \approx \delta \qquad (14)$$

combining Equations 12, 13, and 14

$$\delta \approx v_i \left(\frac{1}{2\rho n^2}\right) \qquad (15)$$

Substituting for n from Equation 11

$$\delta \approx \frac{v_i}{2\rho}\left(\frac{ev_e}{j}\right)^2 \quad \text{to} \quad \frac{v_i}{2\rho}\left(\frac{ev_i}{j}\right)^2 \qquad (16)$$

15

So far, flow has not been introduced so the above equation is general. Taking flow into account, the following notation will be used:

$\delta_u \equiv$ anode extension in flowing gas

$\delta_o \equiv$ anode extension with no flow

$\delta* \equiv$ flow value normalized by no flow value $(\frac{\delta_u}{\delta_o})$

Typical flow velocities in practice range up to about $1\text{-}2\times10^4$ cm/sec. Typical ion drift velocities in atmospheric air at the outer limits of the anode extension ($E/P = 25,000/760 \approx 33$) also run in the neighborhood of $5\text{-}8\times10^4$ cm/sec.

Defining the slip parameter $S \equiv u/v_i = \frac{u}{k_i E}$, significant flow effects can be expected when the slip parameter is of order one, especially in a dense collision dominated discharge where the mean neutral gas motion is easily transfered to the ion population. As can be seen in the specific example,

$$S \equiv \frac{u}{k_i E} \approx \frac{1\times10^4}{8\times10^4} - \frac{2\times10^4}{5\times10^4} \approx .13 - .4 \stackrel{<}{\sim} 1 \qquad (17)$$

and substantial space charge redistribution should be anticipated.

Going back to Equation 16, and rewriting to include flow effects, we have

    a. No electron/ion coupling:

16

$$\delta_u = \frac{(v_i+u)}{j_u^2}v_e^2\left(\frac{e}{2\rho}\right) = \frac{k_iE(1+S)v_e^2}{j_u^2}\left(\frac{e}{2\rho}\right) \tag{18}$$

$$\delta_o = \frac{v_iv_e^2}{j^2}\left(\frac{e}{2\rho}\right) = \frac{(k_iE)v_e^2}{j^2}\left(\frac{e}{2\rho}\right) \tag{18a}$$

and

$$\delta* = \frac{\delta_u}{\delta_o} = \frac{(1+S)}{j*^2} \tag{18b}$$

b. Heavy electron/ion coupling (high space charge fields):

$$\delta_u = \frac{(v_i+u)^3}{j_u^2}\left(\frac{e}{2\rho}\right) = \frac{(k_iE)^3(1+S)^3}{j_u^2}\left(\frac{e}{2\rho}\right) \tag{19}$$

$$\delta_o = \frac{v_i^3}{j^2}\left(\frac{e}{2\rho}\right) = \frac{(k_iE)^3}{j^2}\left(\frac{e}{2\rho}\right) \tag{19a}$$

and

$$\delta* = \frac{(1+S)^3}{j*^2} \tag{19b}$$

where $\qquad j* = \dfrac{j_u}{j_o}$.

From these considerations it can be seen that the power of the velocity term (1+S) will vary with space charge density (or current) and we will write a generalization of 18b and 19b as follows:

$$\delta* = \frac{(1+S)^m}{j*^2} \tag{20}$$

17

where   m   is a variable exponent.

Since continuity considerations require that the total current passing any equipotential surface within the discharge be constant the total current can be represented by the electron current entering the anode where ion contributions are zero, so

$$j = j_o e^{\bar{\alpha} x_c} \simeq j_o e^{\bar{\alpha} f(\delta) \delta} \tag{21}$$

where j_o is the electron current flowing into the ionization region (defined by x_c which is proportional to δ) , the exponential is the multiplication factor, and   f   is an as yet unspecified function of δ , therefore -

with flow:
$$j_u = j_{ou} e^{\alpha_u f \delta_u} \tag{22a}$$

no flow:
$$j_o = j_{oo} e^{\alpha_o f \delta_o} \tag{22b}$$

then
$$j^* = j_o^* e^{f \alpha_o \delta_o (\alpha * \delta * - 1)} \tag{23}$$

NOTE: The * value of a quantity is used consistently to indicate the value of that quantity in a flow field normalized by its no flow value (except for pressure - P* to be introduced later is equal to P/P_o = local value/value at STP $\equiv$ 760 TORR).

18

The function $f(\delta)$ has been introduced to relate the critical ionization distance (that point at $E(x) = E_{APPLIED} + E_{SPACE\ CHARGE} \approx E_i$) to the anode extension δ. It is apparent that δ is proportional to x_c i.e., as δ increases either due to convection or increasing applied voltage, x_c also increases due to increased applied or displaced space charge field, and conversely, as the anode extension shrinks, x_c will decrease. However, due to the non-linearity of the fields involved, a variation in δ will not produce a linear change in x_c. To account for the non-linearity, $f(\delta)$ is assumed to obey a simple power law form

$$f \equiv C\delta *^{n} \tag{24}$$

Squaring $j*$ and substituting into Equation 20, yields the following:

$$\delta* = \frac{(1+S)^m}{j_o^{*2}\exp\left[(2C\delta^{*n}\alpha_o\delta_o(\alpha*\delta*-1)\right]} \tag{25}$$

Rearranging and taking the natural log of both sides,

$$\ln\delta* + 2\alpha_o\delta_o\delta^{*n}(\alpha*\delta*-1) = m\ln(1+S) - \ln j_o^{*2}$$

and solving for δ^{*n} and collecting $\delta*$ terms on the left side,

$$\delta^{*n} - \frac{\delta^{*n-1}}{\alpha*} + \left(\frac{1}{2C\alpha_o\delta_o}\right)\frac{1}{\alpha*}\ln\delta* = \left(\frac{1}{2C\alpha_o\delta_o}\right)\frac{m}{\alpha*}\ln(1+S) - \ln j_o^{*2} \tag{26}$$

19

This is the basic anode extension equation in a flow field, where again the * values are the flow values compared to the no flow values, i.e.:

$$\delta* = \delta_u/\delta_o \quad \equiv \text{normalized anode extension}$$

$$\alpha* = \alpha_u/\alpha_o \quad \equiv \text{normalized ionization coefficient}$$

$$S = u/v_i \quad \equiv \text{the ion slip parameter}$$

$$j_o* = j_{ou}/j_{oo} \equiv \text{normalized saturation current}$$

$$C = \text{CONSTANT}$$

The exponent n of $\delta*$ turns out to be a free parameter of the problem whose exact nature is not yet well established, but is under investigation. The parameter m is the power of the velocity term $(1+S)$ which analytically was determined to range from approximately 1 to 3 , although experimental data indicate that occasionally a higher value is required. The reasons for this disparity are also under active investigation.

Inspite of the limitations cited above, this equation, even in its preliminary form (Equation 26) describes all the previously observed breakdown voltage characteristics on the particular apparatus used in the initial tests for various velocities, turbulence levels, and flow orientations tested, even including some seemingly anomalous points in earlier tests which radically departed from the norm as reported in References 3 and 7. The equation also predicts some salient features in the low velocity ranges which had not previously been observed due to strong emphasis on high speed testing. These low velocity features have

20

been confirmed in recent tests and will be described in detail in part 6 of this section of the report.

To check the mathematical correctness of the form of this equation, when there is no flow, $S = 0$, and by definition, the (*) terms $\equiv$ 1 . Therefore, the three $\ln$ terms go to zero, $\alpha* \equiv 1$ and we are left with the identity $0 \equiv 0$ as it should.

The peculiar geometric factors of a problem are all contained in the δ terms. Gas and electric field parameters enter through the α and S terms; and turbulence effects enter through $\alpha*$ as will be explained in the following sections. Secondary electron production processes are included in j_o* .

To obtain a solution to Equation 26, requires some auxilliary equations which are developed below.

4. Auxilliary Equations

a. The no-flow anode extension (δ_o):

The basic assumption of the anode extension model is that the gap breakdown potential is a linear function of the effective gap length, i.e., the actual gap length less the anode extension (which in effect is a portion of the gap already in a state of local breakdown). Therefore:

$$Vb_o \approx d' \approx d - \delta_o = \bar{E}(d - \delta_o) + V_c \tag{27}$$

$Vb_o \equiv$ no flow breakdown voltage

$d' \equiv$ effective gap

$d \equiv$ actual gap length

21

$$\delta_o \equiv \text{no flow anode extension}$$

$$\bar{E} \approx \text{mean electric field in effective gap}$$

$$V_c \equiv \text{corona initiation voltage}$$

For a specific geometry, Vb_o can be calculated from the condition that $E(x) \equiv E_i$ at $x = C \cdot \delta_o$, resulting in

$$\frac{E(x)}{P_o} \approx \frac{E_i}{P} \approx \frac{R}{(R+x)} \frac{E_p}{P} = \frac{R}{(R+C \cdot \delta_o)} \frac{1}{P} \frac{2Vb_o}{R\log(4d/R)} \tag{28}$$

and

$$Vb_o = \frac{E_i}{2} P*(R + C \cdot \delta_o) \log(4d/R) \tag{29}$$

for the hyperboloidal point-to-plane.

An analytical form can also be determined for V_c as in Section 2 by assuming that V_c is a linear function of the point field, i.e., when the region in the vicinity of the point reaches the reduced field strength for ionization. Again for the hyperboloidal point, this results in

$$\frac{E_p}{P} = \frac{2V_c}{PR\log(4d/R)} \approx C_1 \frac{E_i}{P_o} \tag{30}$$

and

$$V_c \approx \frac{C_1 E_i}{2} P*R\log(4d/R) \tag{31}$$

but $\qquad Vb_o - V_c = \bar{E}(d - \delta_o)$

22

and inserting Equations 29 and 31 into 27 yields:

$$\delta_o \approx \frac{d}{P*(\frac{C}{2}\frac{E_i}{E})\log(4d/R) + 1}$$

(32)

b. Ionization Coefficient Equations (α and $\alpha*$):

(1) No Flow – use Equation 6 with 0 subscript:

$$\alpha_o = APe^{-\frac{BP}{E}}$$

(33)

(2) With Flow/Turbulence Effects α_u :

The primary coupling of α with the flow is result of pressure/density fluctuations in a highly turbulent flow. Therefore, by substituting $P \pm \Delta P$ into the above equation and taking a simple average $\left[\alpha(P+\Delta P) + \alpha(P-\Delta P)\right]/2$, and eliminating second order terms results in –

$$\alpha_u \approx \frac{\alpha_o}{2}\left[e^{\frac{B\Delta P}{E}} + e^{\frac{B'\Delta P}{E}}\right]$$

(34)

or

$$\alpha* = \frac{\alpha_u}{\alpha_o} = \frac{1}{2}\left[e^{\frac{B\Delta P}{E}} + e^{\frac{B\Delta P}{E}}\right]$$

(35)

The pressure fluctuations due to turbulence can be related to the mean flow velocity through the local pressure-density relation in an incompressible flow, i.e., the total pressure equals the sum of the static and dynamic pressures.

23

$$P = P_o + \frac{1}{2} \rho u^2 \qquad (36)$$

Assuming local test section total pressure remains constant in the presence of turbulence, and that $\sqrt{\overline{u'^2}}$, the fluctuating component of velocity, is proportional to $\bar{U}$, the mean flow velocity, then

$$P - P_o = \Delta P \approx \xi \rho \overline{u'^2} \qquad (37)$$

The quantity $(\sqrt{\overline{u'^2}}/U)$ is called the turbulence intensity (Reference 18). At constant temperature, $\rho \sim P$; therefore for constant T ,

$$\Delta P \approx \xi \rho \bar{U}^2 \qquad (38)$$

but also

$$S = U/k_i E \to U = Sk_i E$$

$$u/k_i E \to u \equiv \bar{U} = Sk_i E$$

$$k_i = k_o \frac{P_o}{P}$$

and

$$\Delta P = \xi P(Sk_i E)^2 \qquad (39)$$

Substituting into Equation 35 yields finally -

$$\alpha^* = \frac{1}{2} \left[e^{B\xi P_o k_o \frac{S^2 E}{P^*}} + e^{-\frac{B\xi P_o k_o^2 S^2 E}{P^*}} \right] \qquad (40)$$

which when $u \equiv \bar{U} \equiv S \equiv 0$, reduces to $\alpha^* = 1$ as it should.

24

c. Breakdown Voltage Equation with Flow and Turbulence

The ultimate objective of the above derivations is to arrive at an expression for computing the fundamental gas dynamic effects on the breakdown voltage of an electric discharge. Approximating the breakdown voltage ratio as

$$Vb* = \frac{Vb_u}{Vb_o} \approx \frac{d - \delta_u}{d - \delta_o} \qquad \text{from Equation 27 ,} \qquad (41)$$

then in final form,

$$Vb* = \frac{1 - (\frac{\delta_o}{d})\delta*}{(1 - \frac{\delta_o}{d})} \qquad (42)$$

which also reduces to $Vb* = 1$ when $U = 0 \rightarrow \delta* = 1$.

It should also be noted that when $\delta* \rightarrow 0$, $Vb*)_{max} \rightarrow \dfrac{1}{1 - \frac{\delta_o}{d}}$, the same relation which was postulated in Reference 3 based on the anode extension concept.

d. Summary of Equations

For convenience of reference in the following discussion, the basic breakdown potential and auxilliary equations are repeated below :

25

(1) Normalized Anode Extension $\delta* = \dfrac{\delta_u}{\delta_o}$:

$$\delta*^n - \frac{\delta*^{(n-1)}}{\alpha*} + \left(\frac{1}{2C\alpha_o\delta_o}\right)\frac{1}{\alpha*}\ln\delta* = \left(\frac{1}{2C\alpha_o\delta_o}\right)\frac{m}{\alpha*}\ln(1+S) - \ln j_o*^2 \qquad (26)$$

(2) No Flow Anode Extension δ_o :

$$\delta_o = \frac{d}{P*\left(\frac{C}{2}\cdot\frac{E_i}{E}\right)\log(4d/R) + 1} \qquad (32)$$

(3) No Flow Ionization Coefficient α_o :

$$\alpha_o = APe^{\frac{BP}{E}} \qquad (33)$$

(4) Normalized Ionization Coefficient $\alpha* = \dfrac{\alpha_u}{\alpha_o}$:

$$\alpha* = \frac{1}{2}\left[e^{\frac{B\xi P_o k_o^2 S^2 E}{P*}} + e^{\frac{-B\xi P_o k_o^2 S^2 E}{P*}}\right] \qquad (40)$$

(5) Normalized Breakdown Voltage $Vb* = \dfrac{Vb_u}{Vb_o}$

$$Vb* = \frac{1 - \frac{\delta_o}{d}\delta*}{\left(1-\frac{\delta_o}{d}\right)} \qquad (41)$$

26

5. Qualitative Discussion of the Equations

The key to a clear understanding of the equations lies in a
simple analysis of the normalized anode extension $\delta*$. The basic form
of this equation is

$$\delta* \approx f\left(\frac{S}{\alpha*}\right) \tag{43}$$

In fact it was derived from Equation 20.

$$\delta* = \frac{(1+S)^m}{j*^2}$$

But $S \sim u$ and $j*^2 \sim n*^2$ which gives

$$\delta* \sim L_x \sim \frac{u^m}{n*^2} \tag{44}$$

which is essentially the relationship derived in Reference 3. Thus, the
anode extension is a product of two factors, the pure convective velocity
which, in normal flow, tends to lengthen $\delta*$, and the inverse of the
charged particle density, which tends to shorten $\delta*$ due to faster
recombination at higher $n*$ and consequently results in less particle
drift.

In the reverse flow mode, the $\delta*$ equation can be approximated
by:

$$\delta* \simeq (1+S)^m \tag{45}$$

where u and therefore S are negative, which decreases δ^* in a rapid fashion with increasing negative velocity. It is interesting to note that in the reverse flow approximation, α^* cancels out and V_b^* is not influenced by turbulence.

The breakdown voltage behavior is opposite in sense to δ^*, so when δ^* increases, V_b^* decreases and vice-versa. Note: frequent reference to Figure 6 will be helpful in interpreting the following. As mentioned in the reverse flow mode, δ^* is quickly reduced and therefore, V_b^* immediately rises (Part 2 of Figure 6) and quickly approaches an asymptotic limit (Part 1 of Figure 6) as $\delta^* \to 0$ corresponding to the requirement to breakdown the entire physical gap.

In the normal flow mode (flow from anode to cathode), the initial low gas velocity tends to lengthen δ^*, which causes a decrease in break-down voltage (Part 4 of Figure 6), but due to the exponential dependence of n^*, j^*, and α^* on U (through S), with effective turbulence the α^* terms in the denominator of Equation 26 soon prevail, causing δ^* to decrease and V_b^* to increase at higher velocities and turbulence levels (Part 5 of Figure 6). The velocity at which this transition occurs is a direct function of the effectiveness of the turbulence introduced. If the turbulence is inhomogeneous or ineffective, the V_b^* curve may not reach a minimum in which case, further increases in velocity may actually reduce power input to the discharge (Part 7 of Figure 6, dashed curve extension).

It is interesting to note also that in the normal flow mode with effective turbulence, after initially increasing, δ^* can again approach 0 as its absolute limit (Part 6 of Figure 6) due to the high recombination rate, thereby confining the normal flow V_b^* rise to the same asymtotic

28

limit as applies in the reverse flow case, and again corresponding to the requirement to breakdown nearly the entire physical gap.

It should also be noted that this asymptotic behavior, which has been observed in many cases, (References 2 and 3), poses a fundamental limitation on the stabilization of the discharge potential by gas dynamic means. The final breakdown may possibly be the result of either of two separate sequences:

(a) the relatively uniform external "drift" field may reach such a high value that a random electron avalanche originating in the vicinity of the cathode can take enough energy from the field to completely cross the interelectrode gap, resulting in an internal breakdown of the gas, or,

(b) if the cathode material has a low work function it may begin emitting numerous secondary electrons prior to the drift field reaching the gas breakdown potential in which case the breakdown probability will rise and a cathode limited breakdown may occur.

As turbulence intensities are increased for a given gap length, the reverse flow region is virtually unaffected, except to hasten the rise of V_b* to the asymptote, while in the normal flow direction, increasing turbulence results in higher $\alpha*$ values with an eventual upswing in V_b* due to the resultant $\delta*$ reduction. Figure 7 illustrates the progressive modification of the V_b* curves with increasing turbulence. The asymptotic behavior observed at high normal velocities and turbulence levels confirms the apparent rise in the V_b* curve and explains logically the apparently anomalous "short gap, high current" data points reported in References 3 and 7.

29

The analytic solutions illustrated in Figure 7 also provided an additional area for test and verification of the breakdown equations. It can be seen from the Figure that even in the "short gap, high current" cases, there should be at least a small region of decreasing Vb^* at very low normal flow velocities due to the non-turbulent convective effect. Recent low speed tests have confirmed this characteristic as the data in Figure 8 show.

Another qualitative assessment of the equations can be made by observing the behavior of the curves as a function of the gap length. Figure 9 illustrates this behavior for a 1 and 5 centimeter gap which encompasses the ranges tested. The trends of the curve shift in both normal and reverse flow with changing gap length were as indicated by the theoretical curves.

Section 6 provides a more quantitative comparison of observed data and the appropriate theoretical curves. However, before moving into that subject, a very interesting and rather striking qualitative comparison can be made of the form of Equation 26 and Meek's Breakdown Criterion (as presented in Reference 12) for the uniform field in a static (non-flowing) discharge. As will be seen, despite the very different conditions in the two discharge situations, and the very different approaches used in deriving the breakdown criteria, the resulting breakdown equations are remarkably similar.

Since a description of the non-uniform field anode extension has already been developed, a short description of the Meek-breakdown scenario in the uniform field will help put the remainder of this section in

30

perspective. The Meek Criterion is based on the relative space charge field strength at the head of an electron avalanche compared to the applied electric field. If the avalanche travels a certain critical distance under the influence of the applied field, the space charge field at the surface of the space charge region will become the same order of magnitude as the applied field. When the field ratio $K \equiv E_R/E \rightarrow 0.1-1$, corresponding to the avalanche traveling the critical distance x_c, the space charge field can no longer be ignored. The Meek Criterion from Reference 12 is written as follows:

$$\alpha x + \ln\frac{x}{p} = 14.46 + \ln\frac{KVb}{pd} - 0.5\ln px + \ln x \qquad (46)$$

The method of solution and some results are discussed in detail in the reference. What we will concentrate on are some straight forward substitutions into the above equation for comparison with the anode extension model. If the gap length is adjusted such that an avalanche becomes critical just as it reaches the anode, then the electric field lines will be distorted in the direction of the space charge, as in Figure 10a and the concentration of charge will produce a non-uniform field and, in fact, just as the avalanche touches the anode, it acts as a small area (like a point) of anode extension. The axial length of this extension is $2r$, but r (the avalanche radius) is proportional to the distance it has traveled, so from $2r \sim \delta \sim x$,

$$x \approx c\delta \qquad (47)$$

31

and it can already be seen that the situation looks very much like the point-to-plane geometry. After making this substitution, and then rearranging and substituting non-dimensionalized flow variables for all the quantitites, the result is

$$\delta* - \left(\frac{1}{c\alpha_o \delta_o}\right)\frac{1}{\alpha*}\ell n\delta* = -\left(\frac{2}{c\alpha_o \delta_o}\right)\frac{1}{\alpha*}\ell nS + \left(\frac{1}{c\alpha_o \delta_o}\right)\frac{1}{\alpha*} - \left(\frac{2c}{\alpha_o \delta_o}\right)\frac{1}{\alpha*}\ell n\left(\frac{\alpha_o \alpha* kp^{\frac{1}{2}}}{u}\right) \quad (48)$$

- compare with Equation 26 for the non-uniform flow field -

$$\delta*^n + \left(\frac{1}{2C\alpha_o \delta_o}\right)\frac{1}{\alpha*}\ell n\delta* = \left(\frac{1}{2C\alpha_o \delta_o}\right)\frac{1}{\alpha*}\ell n(1+S) - \frac{\delta*^{(n-1)}}{\alpha*} - \ell n j_o*^2 \quad (26)$$

The transformed Meek Criterion looks very much like equation 26 with some sign changes, but the basic form is nearly identical to the non-uniform flow field equation. The sign changes can be accounted for by the observation that in the non-uniform field equation:

$$\delta_o \approx \frac{1}{\log(4d/R)} \quad (49)$$

and as the point radius (sphere or wire to plane equations are similar) $R \to \infty$, the log term becomes negative and the equations merge to nearly the same form.

After seeing how similar the actual physical situations are at breakdown though, the similarity should not come as a surprise. In fact, what the similarity further suggests is that perhaps there really is no absolute uniform field breakdown. In a uniform gap at a potential just

32

below breakdown, statistically, numerous small electron avalanches may originate and die out in a short distance as depicted in Figure 10a. Many of these mini-avalanches must meet the anode to form minute deformations of the field there, any one of which, if large enough, can ultimately trigger total gap breakdown similar to the non-uniform point-plane.

This brings us to an interesting obeservation concerning a highly non-uniform field situation where the accumulation of space charge around a positive point tends to distort its apparent shape and radius, the result of which is to tend to reduce the non-uniformity and go toward a more uniform field configuration. From these two examples, it would appear that the "natural" state at breakdown in a discharge is a moderate state of non-uniformity rather than at either extreme.

6. Quantitative Comparison of Data and Theory:

Figures 11 through 17 present some typical data recorded on various runs with the point and wire-to-plane electrodes. Conditions ranged from high reverse flow velocities (~120 m/s) to high normal flow (80-100 m/s with turbulence). No turbulence could be introduced in the reverse flow mode, since as illustrated in Fig. 1, the cathode is constructed of aluminum honeycomb flow straightener which assures smooth laminar reverse flow throughout the velocity range tested.

The data presented were collected over a six week period in varying weather conditions and are not corrected for relative humidity and ambient temperature effects, both of which affect the properties being measured. Correction for these effects might reduce the scatter evident in various data sets, especially in the composite summary plots. An additional source of statistical scatter due to unequal current flow to

33

various pins or wires may also be significant, especially in a discharge such as ours which is not ballasted to produce uniform current flow from each element. As noted in Ref. 3, however, effective turbulence does cause more uniform activation of all pins and therefore reduces the adverse effects due to no ballast.

Figure 11 displays corona initiation and breakdown voltages with no flow versus gap length for both geometries tested. Theoretical curves are also displayed which were computed from the appropriate equations developed in Section A . These curves display an intersection of the Vb and Vc characteristics at the shorter gap lengths and are very similar in appearance to those presented in Reference 8 for single point-plane geometries. The intersections define what is termed the "existence" region in Reference 8 for the corona discharge. To the left of this point, a corona discharge will not form, and the gap will breakdown (arc) upon reaching the value of Vc . To the right of that point a corona will form which enhances the discharge current. A common empirical expression which has been found to quite closely fit current data for various non-uniform geometries can be written as follows:

$$I = KCV(V-Vc)$$

The initial constants contain geometric and gas parameters. This equation highlights the dependence of I on V and on the difference between the applied and corona initiation voltages. The existence regions for the present configurations are seen to be for -

Points-Plane $d \gtrsim 0.2$ cm

Wires-Plane $d \gtrsim 2.0$ cm.

34

Figure 12 presents a comparison of $Vb*)_{max}$ from Equation 42 when $\delta* \to 0$. Due to power supply limitations, insufficient points were accessible in the wire/plane configuration because of higher breakdown voltage requirements to adequately define the wire/plane curve so only the point/plane data are presented. This curve is interesting in that it shows at longer gaps flow cannot affect breakdown voltage as radically as it does in a short gap. The general trends of the $Vb*$ vs. velocity data taken under similar conditions of humidity and temperature tend to confirm this. However some contradictions are evident and this cannot be considered a conclusive result.

Figures 13, 14, and 15 are comparisons of data and theory for three gap lengths of $Vb*$ vs. velocity . The values of the parameters C, m, n, and turbulence index used in the calculated curves are given. It has been observed that $C = 1.3$, $m = 3$, and $n = 8$ generally result in a good first estimate for the basic curve, and then the turbulence index (input of turbulence intensity) is varied to match the data. In using this technique, it has been observed that long gaps usually require a lower turbulence index even though the actual turbulence being generated at a given velocity is the same as in shorter gaps. One possible explanation for this is that, as pointed out by Reference 2 after the turbulencee being generated is fully developed, it begins to rapidly decay with time and distance, so in a long gap, although turbulence levels entering the discharge region are the same as in short gaps, the turbulence level leaving the discharge will have decayed more, resulting in a lower average turbulence intensity in the longer gap. This would indicate that

a weighting of the turbulence index with gap length may be required. Probe measurements with screen #9 installed in the test tunnel show that at the highest attainable velocities, the turbulence intensity peaks just at the beginning of the discharge region (at the pin tips), which would support the above argument, and which also may be the key to the success of the screen #9 design.

Figures 16 a, b and 17 a and b are summary plots of Vb and Ib data vs. velocity for the points and wires. While many gap lengths and turbulence levels are included under varying ambient conditions, the plots serve to point out the main features and general trends of these parameters with flow and turbulence. The lines on these curves are not calculated, but are drawn in to highlight the basic features of the various data collected and to show the similarity with the theoretical curves displayed elsewhere.

The next section qualitatively examines the wire/plane in more detail.

B. Wire-to-Plane Geometry

1. Qualitative Discussion of Differences from Point-Plane

One of the significant changes in going from the point-plane
geometry to the wire-plane is a major modification in the shape of the
electric field strength distribution across a gap of given dimension and
a fixed applied voltage. While the assumed distribution (proportional to
$x^{-\frac{1}{2}}$) is still "hyperbolic" as illustrated in Figure 3, at the electrode
surfaces the point field is much higher and drops off much more quickly
than a wire field of the same radius at the same potential. Since in
both cases the cathode is grounded, the wire electric field in the drift
region must be higher than that of the point-plane. The wire radii used
in the current research started at 0.08 cm, but it was found that to
operate within power supply capabilities, the wire size had to be reduced.
As a result the wires were incrementally filed down to a wedge shape of
approximately 30° angle and maximum thickness of about 0.05 cm. This
permitted some current enhancement within available power supply limits.

Several things are evident in comparing point and wire distribu-
tions (see Fig. 3). First, for a given gas, the ionization field strength
E_i determines the length of the anode extension δ , so if E_{i_2} is lower
than the point of crossing (point P) of the curves at a given voltage,
δ_w will be greater than δ_p , but if E_{i_1} is higher than this point,
then δ_p will be greater than δ_w . Since as will be discussed later,
the current is a function of δ , this behavior can have important con-
sequences.

Another important characteristic difference of the point and wire
distributions lies in the transition region from the high field to the drift

37

field. The transition is well defined for a sharp point, but becomes very slow and indefinite in wires and points of large radii. This results in a less well defined anode extension in the flatter distributions, which should affect the flow interactions in the loosely bound outer portions of the space charge (δ) region. Changes in the behavior of the δ region with flow should show up as changes in Vb* with velocity. Some major changes in the wire-plane and point-plane Vb* vs. velocity curves have been well documented in the current research. Figure 18 illustrates the basic nature of these changes.

It has been consistently noted that the wire curves, while still exhibiting the low velocity depression of Vb* , almost always take an early (i.e., low velocity) upturn toward the asymptote whether the flow is turbulent or not (Fig. 8). The convective depression, caused by an initial lengthening of δ , is very small, and it is thought that the rapid rise in Vb* is due to a rather large movement and dissipation of loose space charge at the outer limits of the anode extension. In this region, due to the flatness of the E-field, the ion slip parameter ($S = u/k_iE$) can attain a significant value over much of δ at once, with the result that the outer portion of the anode extension actually blows off or becomes too tenuous at low velocity to act as an extension, which then causes a large and rapid rise of Vb* . The asymptotic limits of Vb* in both the normal and reverse flow directions are interpreted again as the requirement to break down the entire physical gap, as in the point-to-plane development.

A third characteristic of the wire geometry is the inherently higher values of electric field in the drift portion of the gap. This increase in the drift field increases the probability that high ionization

38

and streamer activity in the region near the wire will be able to develop and sustain self-propagation through the drift field region to the cathode by the streamer mechanism discussed in most texts on the subject (see References 8, 12, 15, 16) resulting in breakdown. On the other hand, however, in a discharge designed for optimum energy transfer to a laser gas (pumping), the design of the electrodes will to some extent be dictated by this pumping requirement. In practice, a trade-off is required between electrode design optimized for total power input to the gas and that design optimized for best E/N in the drift region for most efficient pumping. In an electric discharge laser cavity, for instance, an input power of 1000 watts/cm^3 means very little if only two percent is going into the lasing states due to an inefficient E/N in the pumping region.

One of the attractive features of the wire-to-plane geometry is the increased ionization volume available continuously along the wire. The point-to-plane ionization volume, on the other hand, is confined to what would amount to discrete points along the wire.

The point-plane produces discrete 3-dimensional axially symmetric multiplication volumes, at each point, while the wire-plane system is a 2-dimensional continuous volume spanning the length of the wires. Most electron multiplication occurs within these volumes, and so it seems as if a wire should produce more current. But the problem is complicated by the electric field distribution which determines the longitudinal dimension and α the multiplication coefficient. As will be seen total current is not a function of α and δ alone, but a function of the product $(\alpha\delta)$ or $(\alpha*\delta*)$ in the flow situation.

2. Total Current Considerations

As pointed out in Part II, Section 3, since the total current at the anode surface is due to electrons entering the anode from the

39

multiplication region (the positive ions being repelled), the total discharge current can be expressed as a function of the number of electrons entering and their drift velocity (the assumption is made that if negative ions are present, they give up their electron, soon after drifting into the high field region; this assumption is supported by Reference 15 and some sample calculations presented in Reference 8).

A single electron entering the high field region will exponentially multiply to produce

$$n = n_o e^{\int_x^o \alpha dx}$$

electrons at the anode surface with $n_o = 1$. Since the current density is the current per unit area,

$$j_e = e n_e v_e = i/A \tag{50}$$

the total current (which must be constant across the discharge) can be expressed as

$$i = i_o^- e^{\int_x^o \alpha dx} = j_e A \tag{51}$$

This allows the total current to be discussed in terms of electrons arriving at the anode. That number is strongly dependent upon how many electrons enter the multiplication region, whether as free electrons, or attached to atoms or molecules as negative ions. The electron input is described as i_o^- in the above equation and is

$$i_o^- = (e n_{e_o} v_e + e n_- v_-)A \equiv \gamma \cdot e \tag{52}$$

40

where

n_{e_o} $\equiv$ free electron density from drift region

n_- $\equiv$ negative ion density from drift region

v_e, v_i $\equiv$ particle drift velocities

A $\equiv$ area through which particles pass into multiplication region

γ $\equiv$ secondary electron supply rate.

Without covering many details or methods already discussed in Section A, the above considerations lead to the normalized current equation below

$$i* = \frac{i_u}{i_o} = \gamma* e^{2C\alpha_o\delta_o\delta_o^{*n}(\alpha*\delta*-1)} \tag{53}$$

where

$\gamma* \approx i_{ou}^-/i_{oo}^-$ $\equiv$ normalized secondary electron supply rate.

From equation 52 it can be seen that the units of γ are electrons/second, and that it is an electron flow rate into the multiplication region. It is the counterpart of the Townsend secondary ionization coefficient in a non-flowing discharge.

Understanding the nature of γ , we are now able to analyze possible flow effects. Electrons coming into the ionization region can arrive in two forms, either as free electrons at the characteristic electron drift velocity which is generally much higher than typical

41

flow velocities, or attached to a heavier particle in the form of negative ions, etc., whose drift velocities and therefore delivery rates can be greatly altered by the flow.

Now we discuss the third component of current, the positive ion contribution. In the determination of total current by counting electrons flying past the anode surface, the positive ions play an indirect role by supplying secondary electrons primarily through impact with the cathode where energetic collions can result not only in neutralization of the ions, but also release of additional electrons which then begin to move toward the anode. These secondary electrons may proceed as free electrons or attach to particles and proceed as negative ions, thus the positive ion contribution shows up as an enhancement of both γ_e and γ_{n-} . Since both positive and negative ion drift velocities are of the same order of magnitude as the flows being discussed, it can be anticipated that the total current would be significantly affected by flow through ion slip - and electron trapping discussed in Part IIA.

Considering the free electron component alone, the total input of electrons to the multiplication zone is, from equation 52

$$i_o^- = (e \, n_e v_e) A \qquad (54)$$

At first it would seem that electron velocity in the drift region should not be significantly affected by the flow due to low electron slip and negligible trapping due to space charges. However

$$v_e \approx k_e E(x) \qquad (55)$$

42

and

$$v_e{}^* = \frac{v_{e_u}}{v_{e_o}} = \frac{k_e}{k_e} \frac{E_u}{E_o} = E^* \tag{56}$$

In nearly all non-uniform geometries, the electric field is given by an expression of the following form -

$$E(x) \approx \frac{1}{x} \frac{cV}{\log(CONST)} \tag{57}$$

with the result that

$$E^*(x) = V^*$$

and at breakdown,

$$E_b^* = V_b^* \tag{58}$$

Therefore from equations 54, 55, and 58 -

$$i_o^* = \frac{i_{ou}^-}{i_{oo}^-} = \frac{n_{eu} v_{eu}}{n_{eo} v_{eo}} = V_b^* n_e^* \tag{59}$$

This equation shows that even free electron velocities can be altered indirectly by flow modifications which affect the breakdown voltage and hence the electric field even in regions where electron trapping is not a significant factor. V_b^* and therefore electron speed can be altered by 30% or more at moderate flow velocities.

Now the total current can be written as follows -

43

$$i* = n_e* \, Vb* \, e^{C\alpha_o \delta_o \delta^{*n}(\alpha*\delta*-1)} \tag{60}$$

The n_e* term is a function of the total current, and all associated secondary electron supply processes such as cathode emission, photoionization, etc., whose variations with flow are as yet undetermined.

In a discharge where many of the secondary electrons are liberated by positive ion impact with the cathode, however, n_e* will be a function of the ion slip and the current equation may assume the following form -

$$i* = Vb* \, \frac{(1+S) + \gamma*}{2} \, e^{C\alpha_o \delta_o \delta^{*n}(\alpha*\delta*-1)} \tag{61}$$

Neglecting $\gamma*$ temporarily, Equation 61 will be used to qualitatively examine the behavior of the breakdown current with flow and turbulence and to attempt to explain some of the observed differences in the point-to-plane and wire-to-plane $Vb*$ and Ib vs. velocity data collected during the current research effort.

Figures 16, 17 and 18 are typical plots of breakdown voltage and current vs. velocity for the point and wire configurations and will be referenced frequently in the following discussion.

a. Point-Plane Current Interpretations

Since breakdown voltage variations with flow were already discussed in detail in Part II.A.5, we will concentrate on some typical point-plane current data first. Beginning at the origin (U=0) in Fig. 17a, it can be seen that, as velocity increases in the normal flow

(positive) direction, the current begins to rise (region 1), reaches a low
maximum (region 2) and then declines slightly (region 3). A typical
V_b^* curve (Fig. 8) shows a depressed breakdown voltage in this region,
which from Equation 61 tends to decrease I_b but the increasing velocity
term helps to compensate for the reduction as does the product $(\alpha^* \delta^*)$ in
the exponential, and the current in regions 1 thru 3 is dominated by the
behavior of δ^* (in this velocity region turbulence intensity is not yet
sufficient to cause significant enhancement of α^*). As velocity increases,
if an effective turbulence generator is in place, α^* becomes dominant due
to its rapid exponential growth with increasing velocity (Equation 40), and
in accordance with Equation 61 an overexponential rise in I_b is noted
(region 4 of Fig. 17a). The figure also shows V_b^* leveling at the normal
flow asymptote which would also cause a leveling of the I_b character stic
or at least a leaning toward a $(1+S)$ linear rise in accordance with Equa-
tion 61.

b. Reverse Flow Current

Interpretation of the reverse flow (negative velocity) current
and voltage characteristics in the point-plane and wire-plane is essentially
the same, so the following discussion applies to both configurations. Since
no turbulence was introduced in the reverse flow mode, other processes tend
to dominate breakdown characteristics in this regime. Equation 45 shows a
rapid decrease in δ^* with reverse flow which causes an equally rapid rise
in V_b^* ; the V_b^* increase and $(1+S)$ velocity term decrease might be
expected to neutralize each other as in the normal flow mode, leaving the
major influence on I_b the δ^* term again. Since δ^* is rapidly decreas-
ing, this line of reasoning would have I_b decreasing at a fairly rapid

45

rate. However, the experimental data consistently show a steep rise
in Ib at relatively low negative velocities (region 5 of Fig. 17a), and
a leveling or decrease at higher velocities (regions 6 and 7). The high
velocity reduction in Ib is easily understood via Equation 61, since the
velocity term (1+S) will eventually approach zero at high enough nega-
tive velocities causing Ib to approach zero. Also since δ^* is con-
stantly decreasing with increasing reverse flow, this tends to reduce Ib
more at high velocity. (In one experimental case Ib was reduced to
approximately 1/10 of its no flow value). It seems that the only factor
going in favor of increasing reverse flow current in the low velocity
region is the increase in Vb* ; but numerical calculations show that the
velocity term more than offsets this factor. Careful review of the equa-
tions brings aid from an unexpected source to explain this strong low
negative velocity current enhancement through the α^* term.

Recalling the form of α from Equation 6, it can be seen that
α is a function of E as well as P , and as Vb* increases in the
reverse flow mode, E also increases, since from Equation 1 E ~ V .
Mathmatically this leads to the following enhancement of $\bar{\alpha}$ due to the
rise of E for the point-plane -

$$\alpha^*(\Delta E) \simeq \exp\{(-BP/Vbo)[(R \log(4d/R)](1/Vb^*-1)\}$$ (62)

Another subtle effect may also come into play here, since, as flow is
directed into the quasi-steady no-flow anode extension region, the initial
hydrodynamic effect will be to promote a flattening and radial spreading
of the dense space charge boundary. In this case the point radius R

46

should be replaced by R_{EFF} which will be a complicated function of the flow and electric fields. Qualitatively, however, it is expected that after initial low velocity spreading which enhances $\alpha*$ (via Equation 62) and therefore $i*$, $i*$ will eventually decline due to the continued decreases in $\delta*$ and the $(1+S)$ velocity term in accordance with Equation 61 and R_{EFF} will also decline. The end result of these processes is a rapid reverse flow current rise and fall as illustrated by Fig. 7a. These two reverse flow effects $\alpha*(\Delta E)$ and $R \rightarrow R_{EFF}$ are not peculiar to reverse flow, but in the normal mode they must compete with other strong influences which may tend to mask their effects except under special circumstances. For example, in the normal mode, gas flow and positive ion repulsion from the anode act in the same direction on the high density positive space charge, so gas convection by itself does not promote radial spreading as it does in the reverse flow mode where electrostatic repulsion and convection oppose each other. If, however, the normal flow becomes highly turbulent, the random gas velocity and density fluctuations in the ionization region tend to enhance ionization and the transport properties of the gas resulting in faster radial diffusion and dynamic spreading of the positive charges, and as in the reverse flow case, the effective radius of the virtual anode is increased. Reference 3 presented photographs of various discharge conditions which visually illustrates this turbulent enhancement, the glow region in the turbulent case being 3-5 times the radius of the no-flow or laminar flow cases.

    c. Wire-Plane Normal Flow Breakdown Current and Voltage

        Breakdown data for this configuration was limited to a short gap length range above the existence point for the corona discharge (~2 cm)

47

due to power supply problems which limited available voltage to approximately 33KV. This limitation effectively restricted wire-plane gap length to 2.8 cm or less with flow. Since this is less than 1 cm into the corona existence region, it is not possible to give a full accounting of flow effects. In general, however, non-turbulent curves were usually flat with little enhancement of current, while most curves with turbulence screen #9 in place showed slow but steady improvement with velocity. One interesting test was performed with a gap length below the corona existence point, and the introduction of turbulent flow resulted in the flow of a small current before breakdown. This is most likely due to the pressure/density fluctuations in the vicinity of the wires which cause corresponding fluctuations in E/P. If the lowest pressure variations result in a high enough value of the reduced field (E/P), some ionization will begin to occur before breakdown.

The wire-plane breakdown voltage curves were mentioned in Section II A.6 and the general trends shown in Figs. 8 and 18. One additional observation will be made here. It has been noted in the point-plane configuration in the normal flow mode, that as gap length is shortened toward the corona existence point, breakdown voltage will rise at lower flow velocities. In the most extreme point-plane case, Vb^* had reached the normal flow asymptote at 40 m/s with no turbulence. In fact the curve looked almost like a wire-plane curve. This seems to infer that if gap length is in the corona existence region, but close to the existence point, the normal flow Vb^* characteristic may tend toward the wire-plane shape of Fig. 18. That is, if the gap is short relative to the corona existence

48

point a low velocity rise in Vb will occur. Additional data at various

gap lengths are necessary to confirm this preliminary observation. If,

in fact, this is a true characteristic, it is most likely related to the

variation of the axial breakdown electric field distribution as the gap

length is reduced.

The remaining sections review requirements for the optimum

pumping of a laser gas mixture vs. electrode geometry, a final over-

view of data and theory developed earlier, and some conclusions and

recommendations for further research.

C. Electrode Design/Optimization

In electric discharges designed for laser pumping, two basic require-
ments must be satisfied. First, the electrodes must efficiently produce
a sufficient electron population to permit effective energy transfer to
the laser gas. Secondly, the electrode design must be such that the
reduced electric field (E/N or E/P) in the pumping region optimizes elec-
tron energy for maximum energy input to the desired vibrational or
electronic energy levels. Degradation in either of these critical areas
will result in reduced laser power output.

Discharge cavity size limitations or specifications will most likely
dictate the maximum gap spacing between anode and cathode, so within that
limitation the combination of the stressed electrode radius and gap length
must be determined which best satisfies the requirements above. Since the
E-field distribution is a function of both parameters, they cannot be
considered separately. In addition, it has been shown that space charge
effects via the "anode extension" and radial spreading cause significant
changes in the "apparent" electrode geometry which should be taken into
account in the final design. The gasdynamic interactions with these space
charge induced dimensional changes, in effect, provides an extra degree of
freedom in a fixed geometry cavity through some control of the radial
spreading and anode extension. This in turn permits, to some extent, ad-
justment of E/N and electron production via flow and turbulence.
Additional benefits arise through the enhancement of transport properties,
improving stability while concurrently increasing electron production.

Calculation of the reduced fields via the adaptation of the hyper-
boloidal point-plane, and an assumed wire-plane distribution indicates

49

E/N values in the drift regions of the discharges tested slightly higher
than the optimum range specified in Reference 1, a condition which can be
remedied by proper adjustment of the geometric parameters, provided that
an adequate power supply is available.

III. SUMMARY

A. Data

The Vb* data for both configurations are quite similar in the reverse flow modes, showing a fast rise to an apparent asymptotic limit (Figs. 16 a,b). This is presumed due to collapse of the anode extension by the gas flow.

The normal flow mode shows Vb* initially decreasing for all gaps and geometries with an eventual upswing which depends strongly on turbulence intensity, and appears to also depend on gap length relative to the corona existence point, with early (low velocity) rise strongly favored in the high turbulence and/or short gap cases (Figs. 8, 16 a, b, 18).

The breakdown current data in the reverse flow illustrated similar behavior in the point and wire-plane configurations, starting with a substantial low velocity rise followed by a decline at higher velocities.

The point-plane normal flow current behavior exhibits several features under various conditions. The most promient of these are outlined in Fig. 17a. Many smaller scale perturbations are evident in some individual sets of data, but the high turbulence, higher current curves seem to follow the same basic pattern in the point-plane configuration. The wire-plane current curves exhibit much more scatter and trends are not as well defined as with the point geometry. This is probably attributable to the fact that data were not accessible in a wide range of gap lengths, but were restricted to gaps close to corona initiation where Vb and Vc are not far apart, and therefore current levels are relatively low.

51

B.   Theory

The theory developed in Part II accounts for the major features of the Vb and Ib curves described above as can be seen in the various figures, but many of the analytical terms can be improved and it is believed that further study will lead to analytic expressions for the various parameters of the theory which have been mentioned. The clear physical basis of the theory lends to easy interpretation of various flow related phenomena and should prove useful in visualization and design of flow-type systems and possibly in trouble-shooting of existing flow system problems.

IV. CONCLUSIONS AND RECOMMENDATIONS

A. Conclusions

1. The basic anode extension model developed herein appears to offer a simple approach to the interpretation and calculation of basic gasdynamic effects on high pressure corona discharges.

2. The flow field interactions discussed are basic, so the approach used in modelling the positive point-plane electrode system should be easily applied to other gap configurations, polarities, gas mixtures, and pressure regimes.

3. A more rigorous evaluation of various terms in the basic model should provide better insight into the dominant forces in various flow regimes, and most likely will result in definition of some of the small scale features not yet well explained.

B. Recommendations

1. Continue data collection on the wire-plane electrode configuration when a larger power supply is available (50KV, 50ma should be sufficient with present hardware).

2. Develop a good analytical expression for the effective electrode radius for insertion into the present point-plane computational model.

3. Include $\alpha^*(\Delta E)$ and radial spreading effects in normal flow computational scheme.

4. Test point-plane in reverse flow mode with turbulence at low velocities to verify Equation 45.

5. Develop comprehensive analysis of flow on γ^* for various types of gas mixtures, i.e., attaching, non-attaching, etc.

53
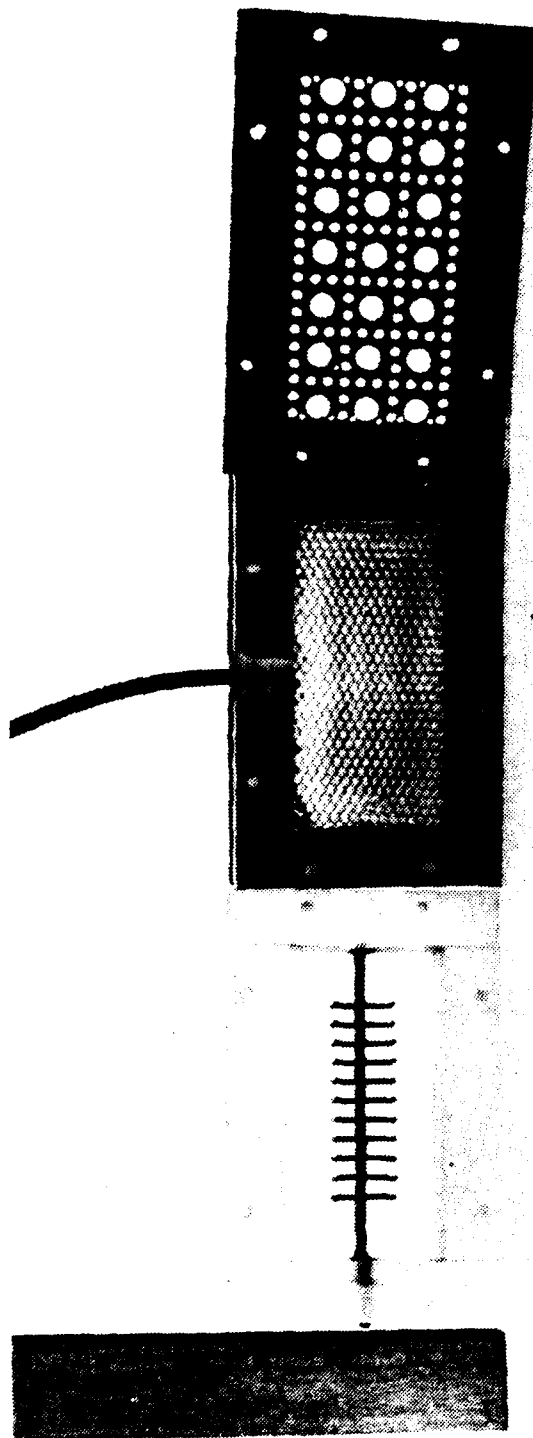
a. Points-Plane - Steel Pins-Anode, Aluminum Honeycomb Cathode
   (Flow Straightening Material), Phenolic Turbulence
   Screen #9.

Figure 1. Electrodes and Turbulence Generating Screen #9.

54
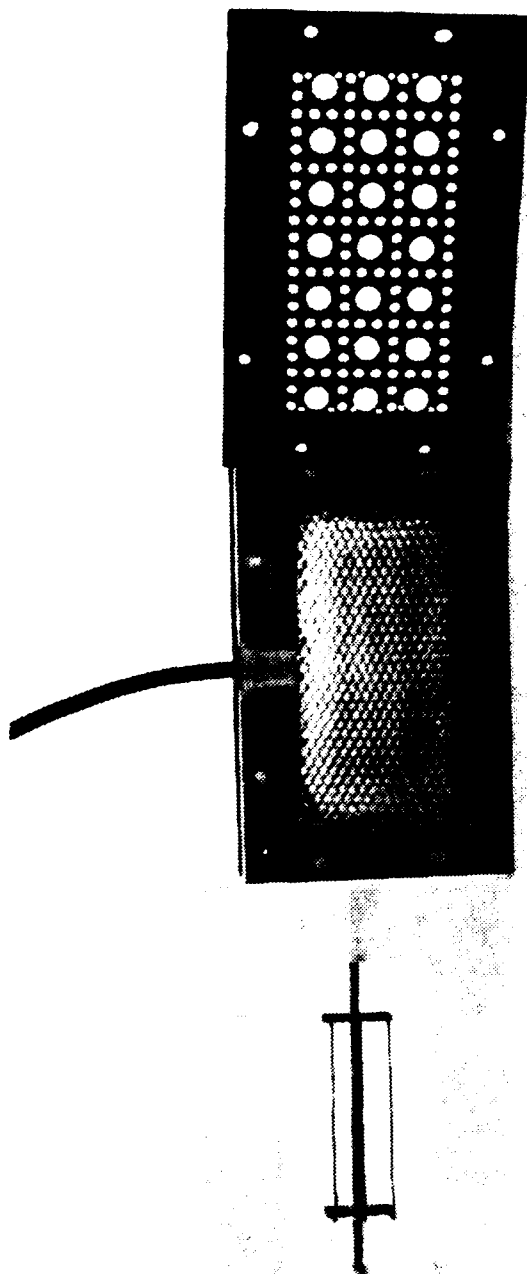
b. Same as Figure 1a with Point Anode Replaced with Thin Steel Wires.

Figure 1. Electrodes and Turbulence Generating Screen #9.

GRID

CATHODE

ANODE

(a)   Normal Flow

CATHODE

ANODE

(b)   Reverse Flow

GRID

CATHODE

ANODE
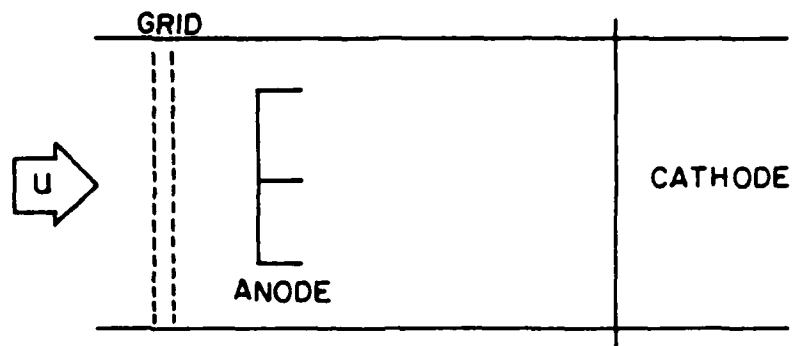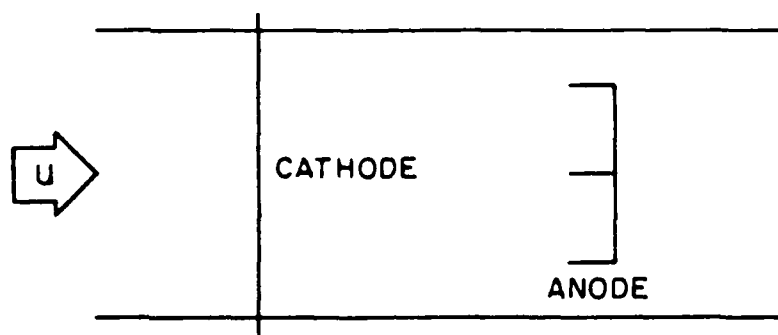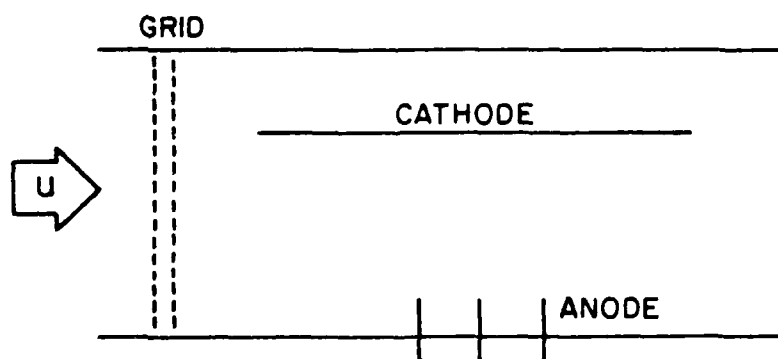
(c)   Cross - Flow

Figure 2. VARIOUS ORIENTATIONS OF ELECTRODES
AND TURBULENCE GRIDS TESTED.

56
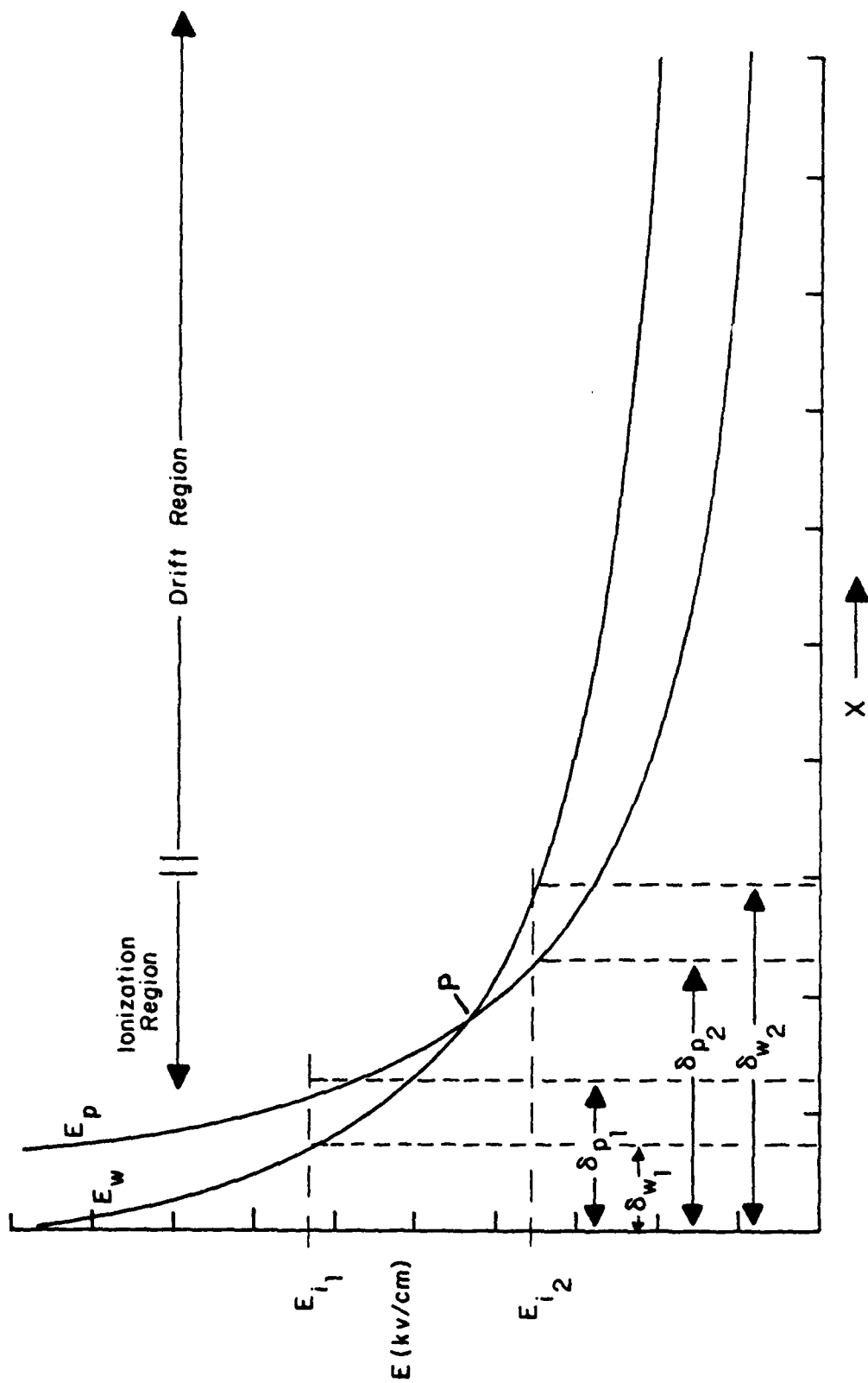
Figure 3. TYPICAL POINT – and WIRE – PLANE ELECTRIC FIELDS.
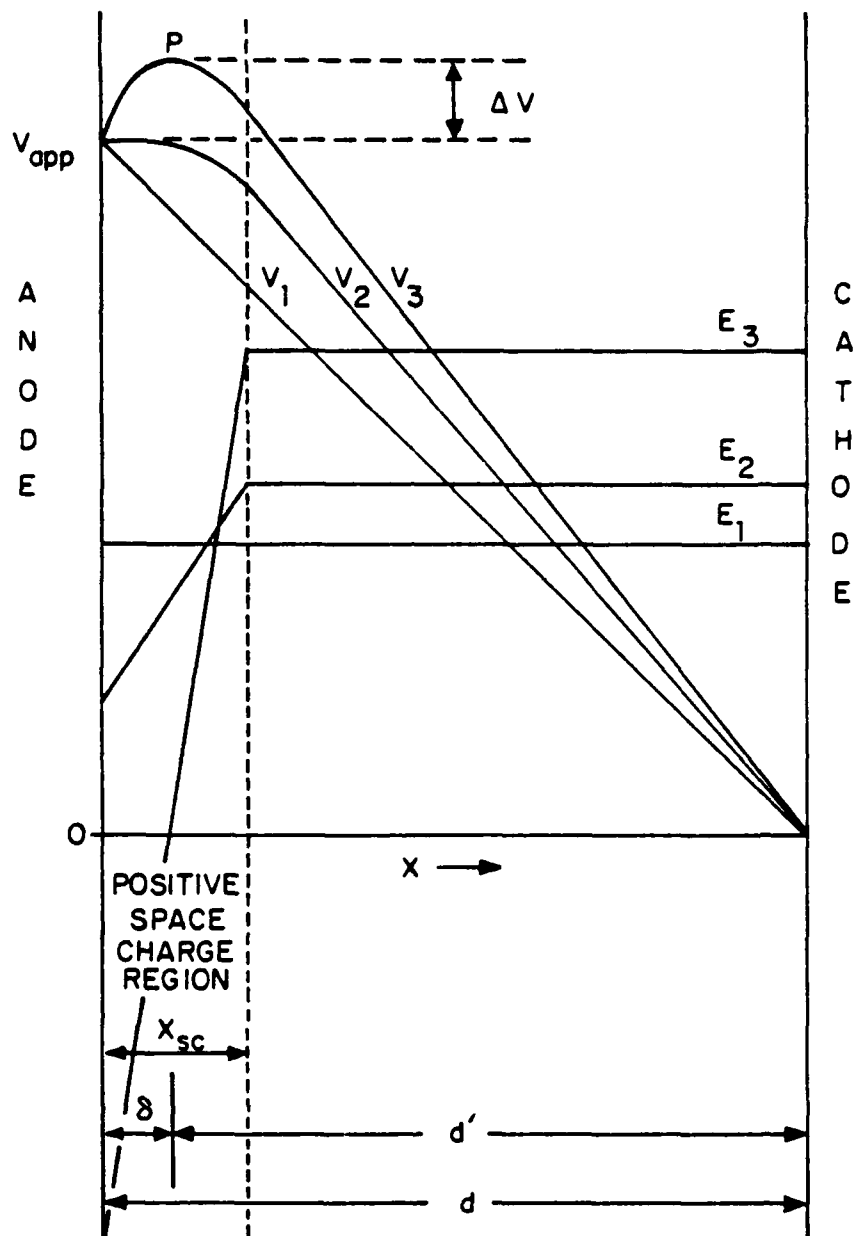
Figure 4. ELECTRIC FIELD AND VOLTAGE DISTRI-
BUTION BETWEEN PARALLEL PLATES.
Subscripts: (1) No Space Charge
(2) Moderate Space Charge
(3) High Space Charge

58

Figure 5. (a) Schematic of Field Lines and Equipotentials.
(b) Apparent Dimensional Changes Due to Space Charge.
(c) Applied, Space Charge and Total Field Distributions.
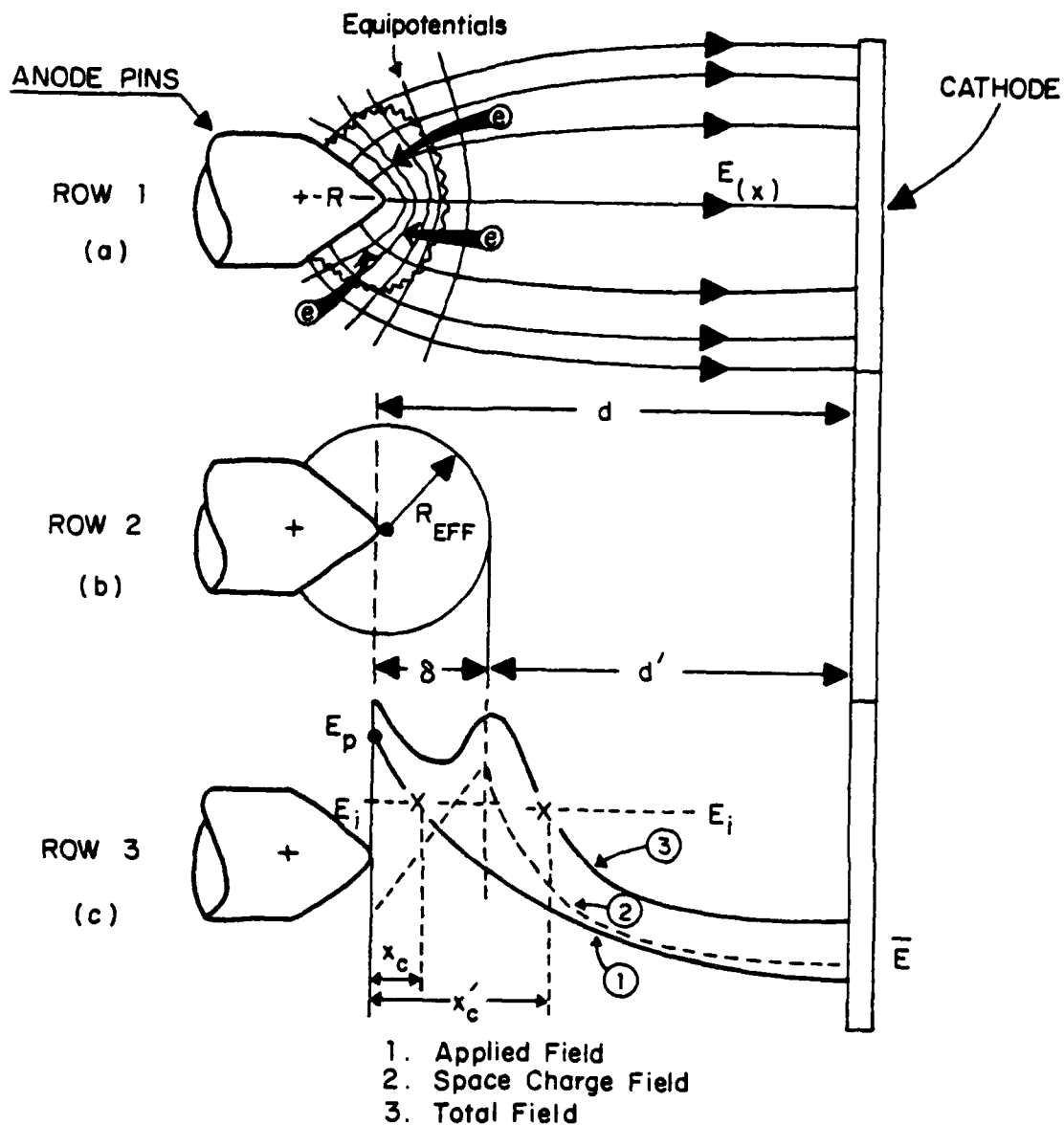
X_c and X_c' are Critical Distances From Anode Where Electron Avalanching Begins $(E = E_i)$ With and Without Space Charge Effects.

59
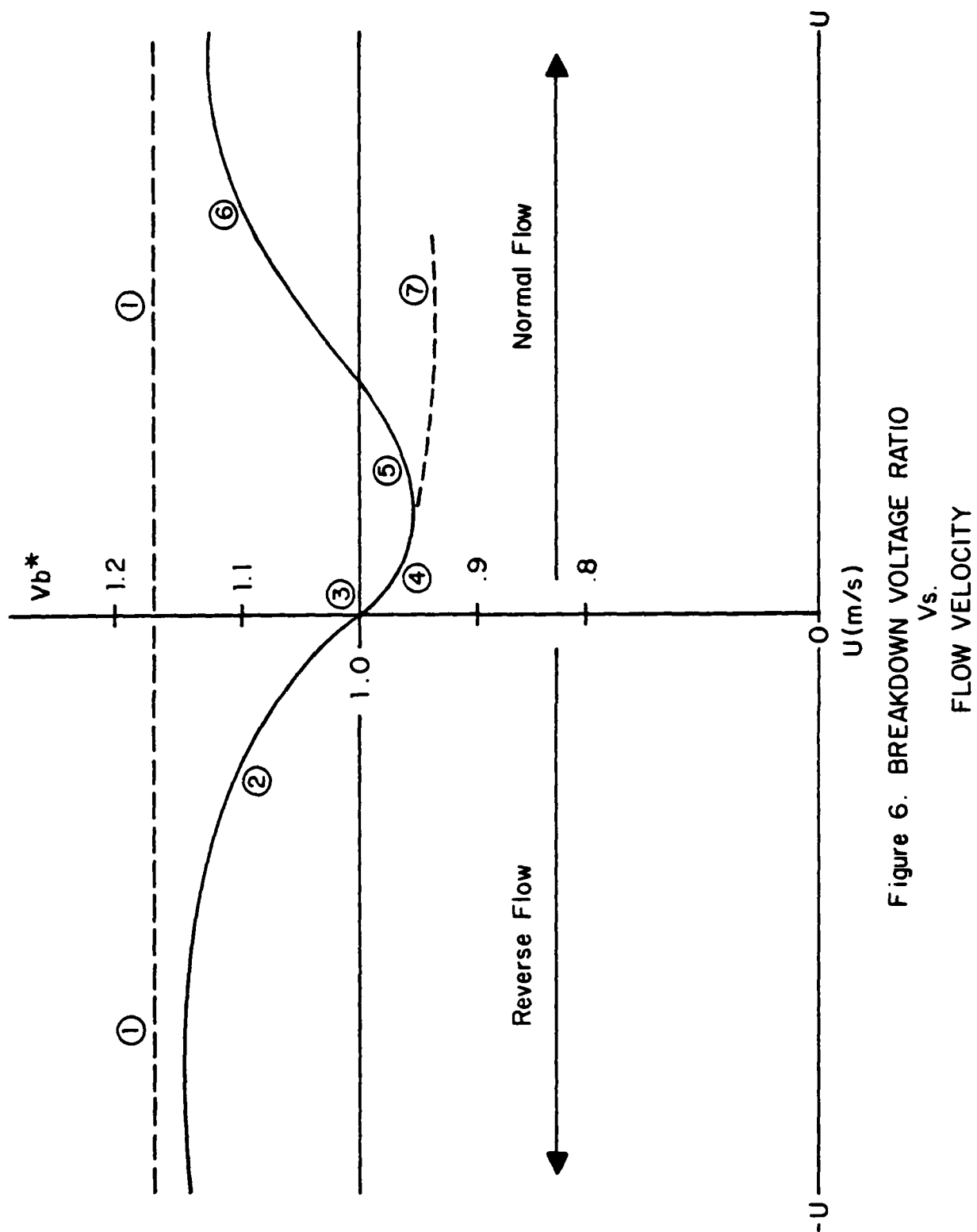
Figure 6. BREAKDOWN VOLTAGE RATIO
Vs.
FLOW VELOCITY

60
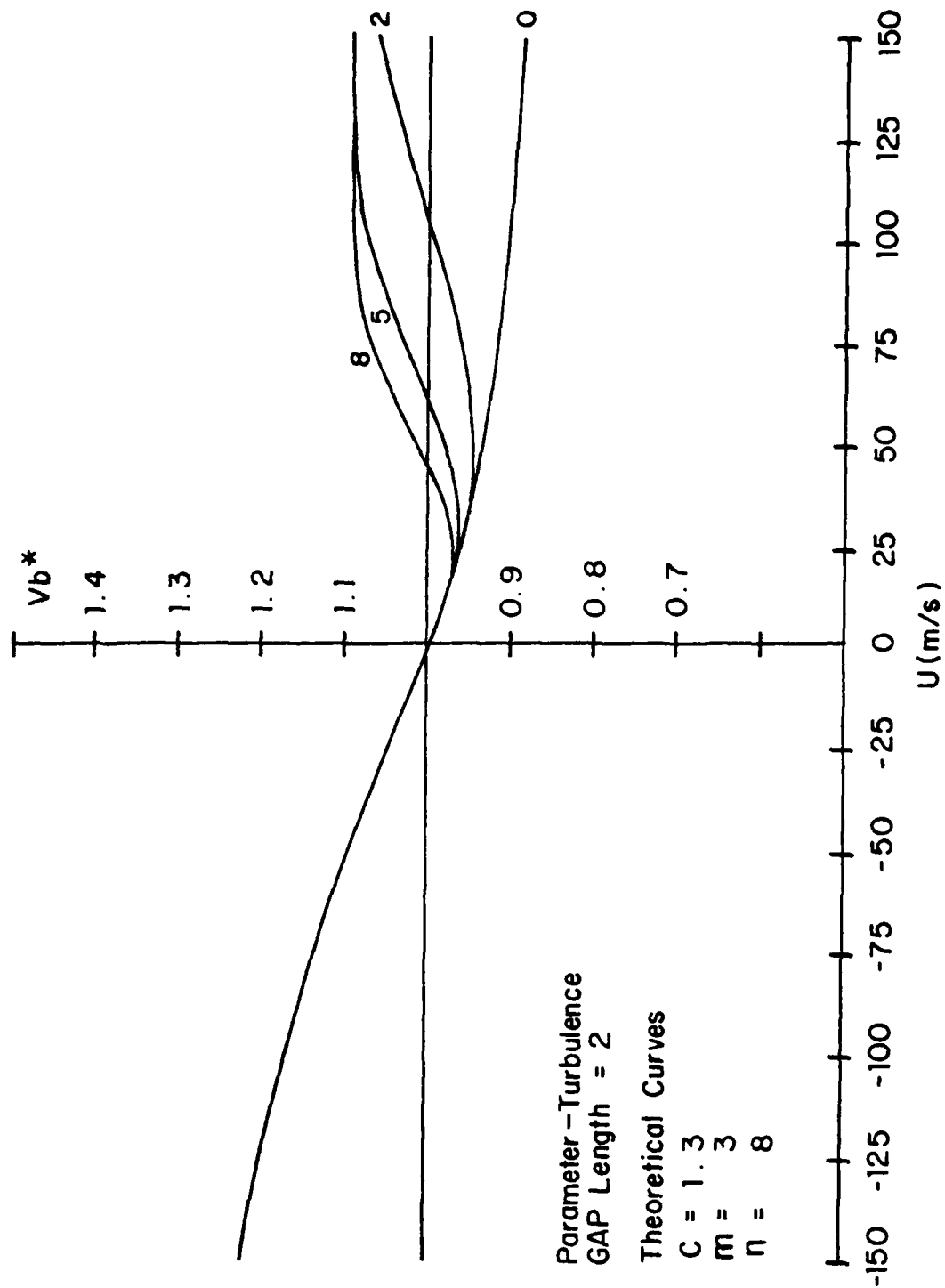
Figure 7. PLOT OF BREAKDOWN VOLTAGE VERSUS FLOW VELOCITY

Parameter — Turbulence
GAP Length = 2

Theoretical Curves

C = 1.3
m = 3
n = 8

61
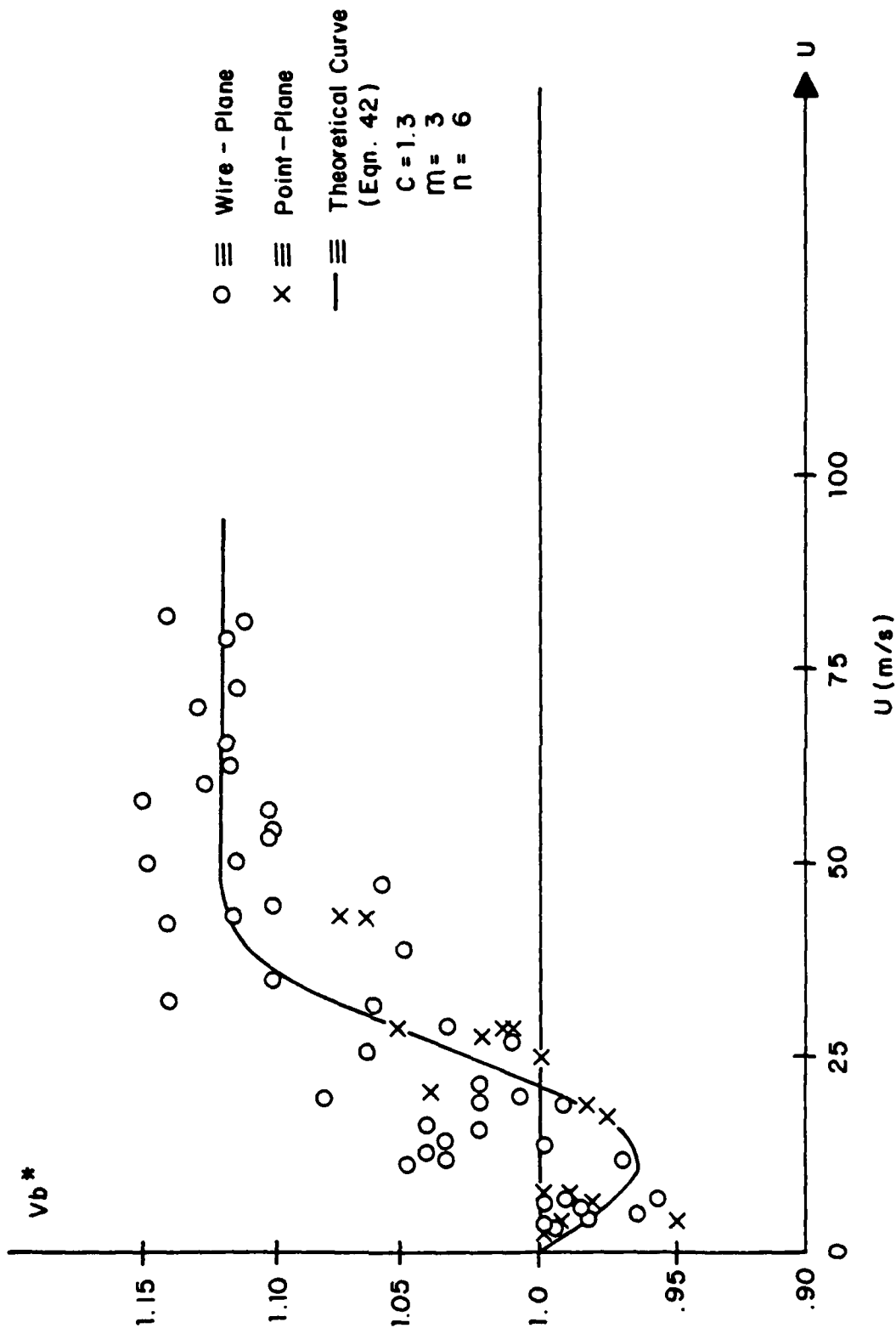
Figure 8. LOW SPEED PLOT OF BREAKDOWN VOLTAGE VERSUS FLOW VELOCITY - NORMAL FLOW.

62

v_b^*

1.4

1.3

1.2

1.1

0.9

0.8

0.7

-100   -75   -50   -25   0   25   50   75   100

U(m/s)

1

2

Turbulence = 50
GAP Length = 1
C = 1.3
m = 6
n = 5
} Curve 1
Theory

Curve 1

Curve 2

Turbulence = 1
GAP Length = 5
C = 1.3
m = 3
n = 8
} Curve 2
Theory
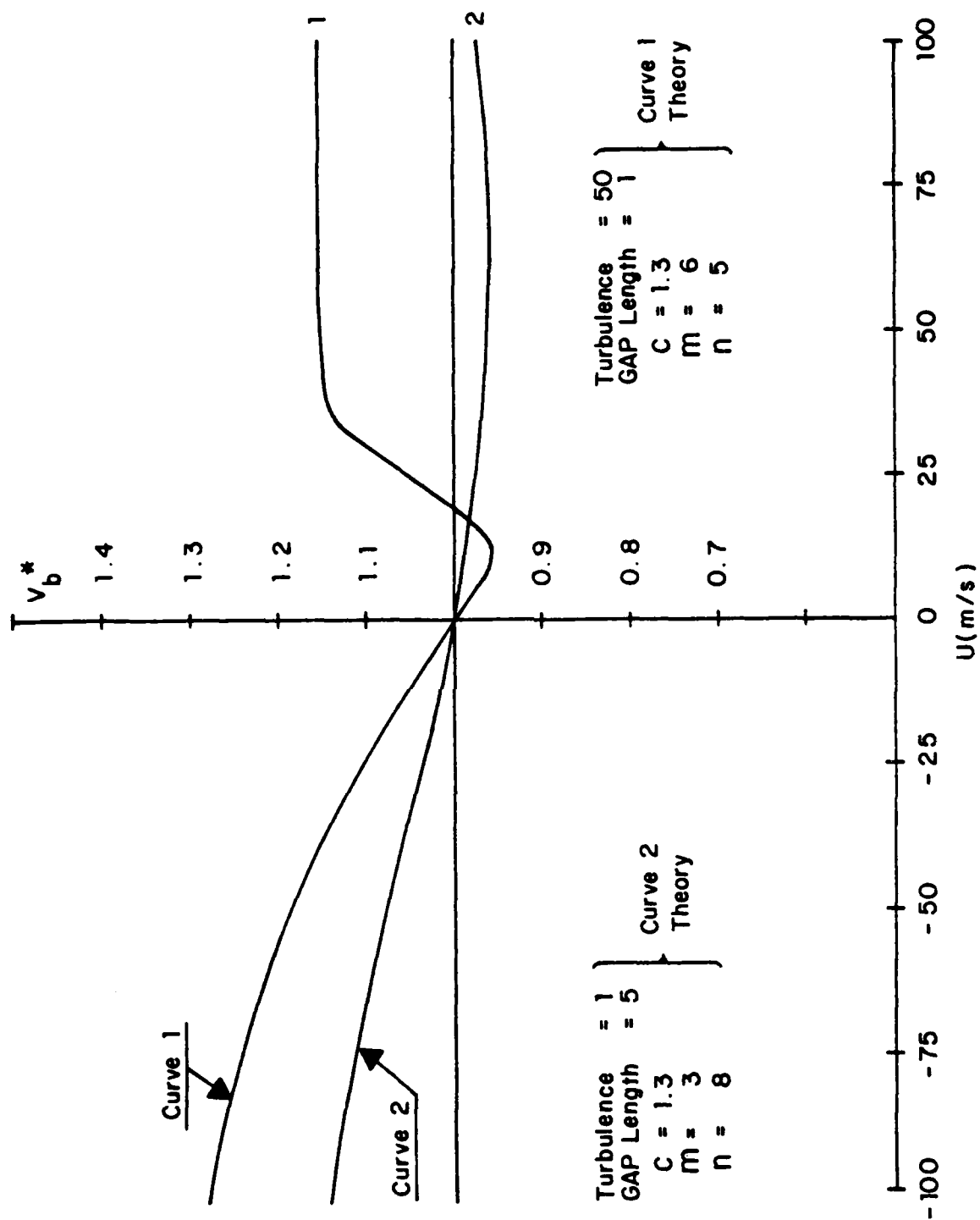
Figure 9. PLOT OF BREAKDOWN VOLTAGE VERSUS FLOW VELOCITY.

63
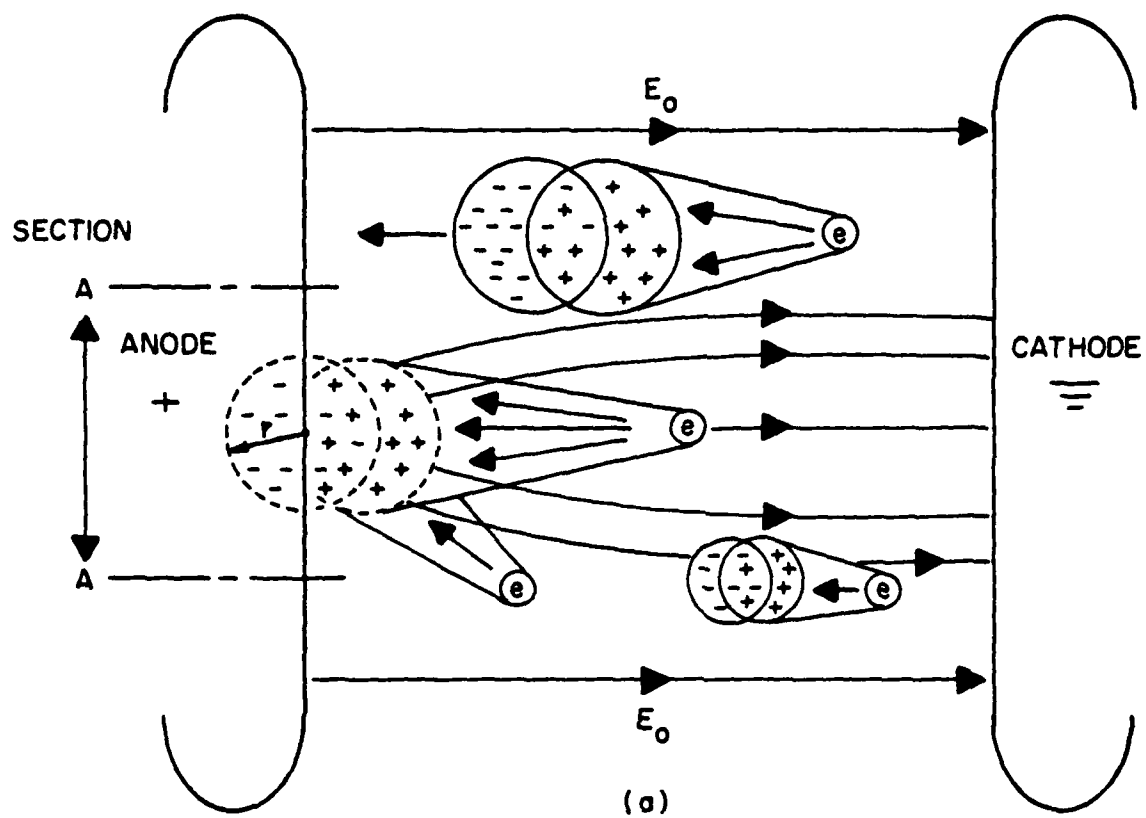
SECTION A-A
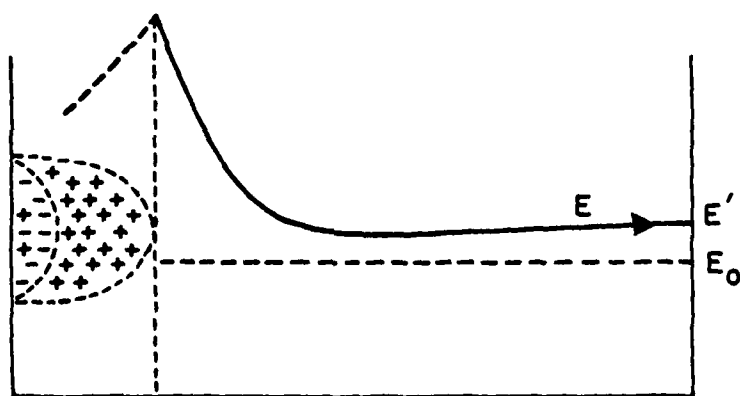
Figure 10.   (a) Activity in a Parallel Plate Gap.
             (b) Modified E-Field Due to Space Charge.

64
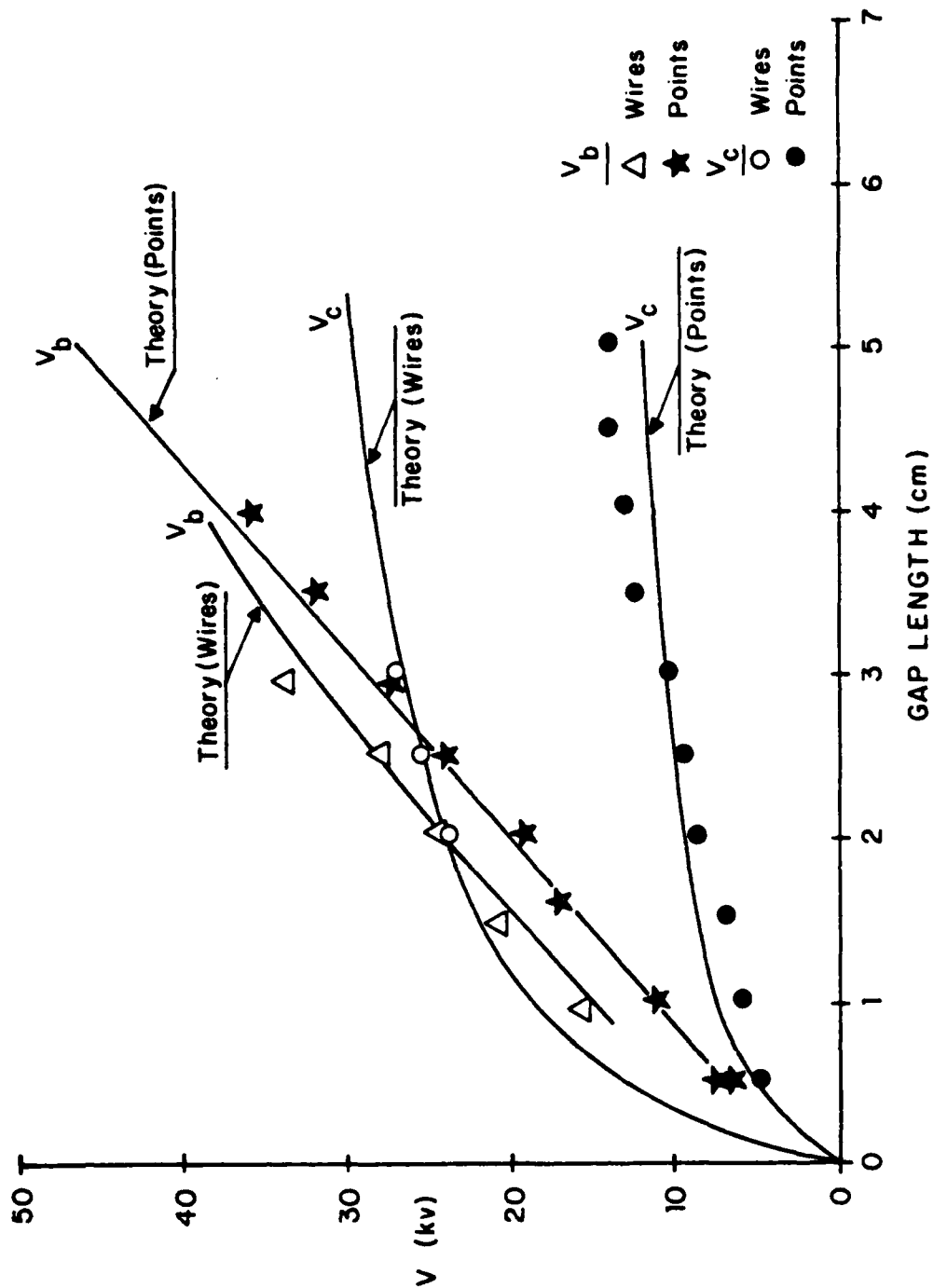
Figure 11. BREAKDOWN AND CORONA INITIATION VOLTAGE Vs. GAP LENGTH FOR NO-FLOW AT ATMOSPHERIC PRESSURE, FOR POINT-PLANE AND WIRE-PLANE GEOMETRIES.
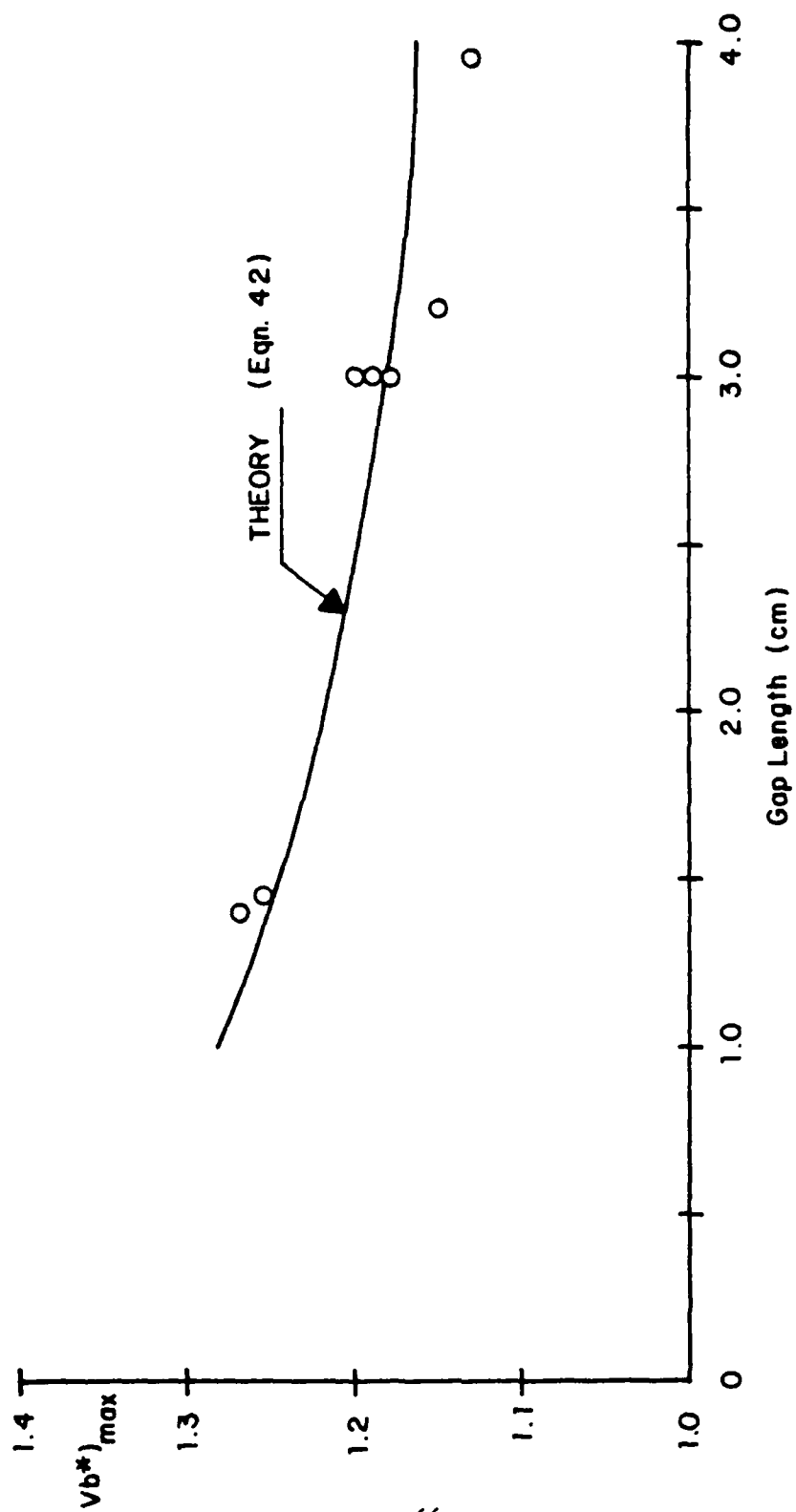
Figure 12. SUMMARY OF MAXIMUM BREAKDOWN VOLTAGE RATIO Vs. LENGTH FOR POINT-PLANE GEOMETRY.

66

Vb*

1.4

1.3

1.2

1.1

0.9

0.8

0.7

U(m/s)

-100 -75 -50 -25 0 25 50 75 100

X ≡ Data Points
— ≡ Theoretical Curve

Turbulence = 13
GAP Length = 1

C = 1.3
m = 3
n = 8
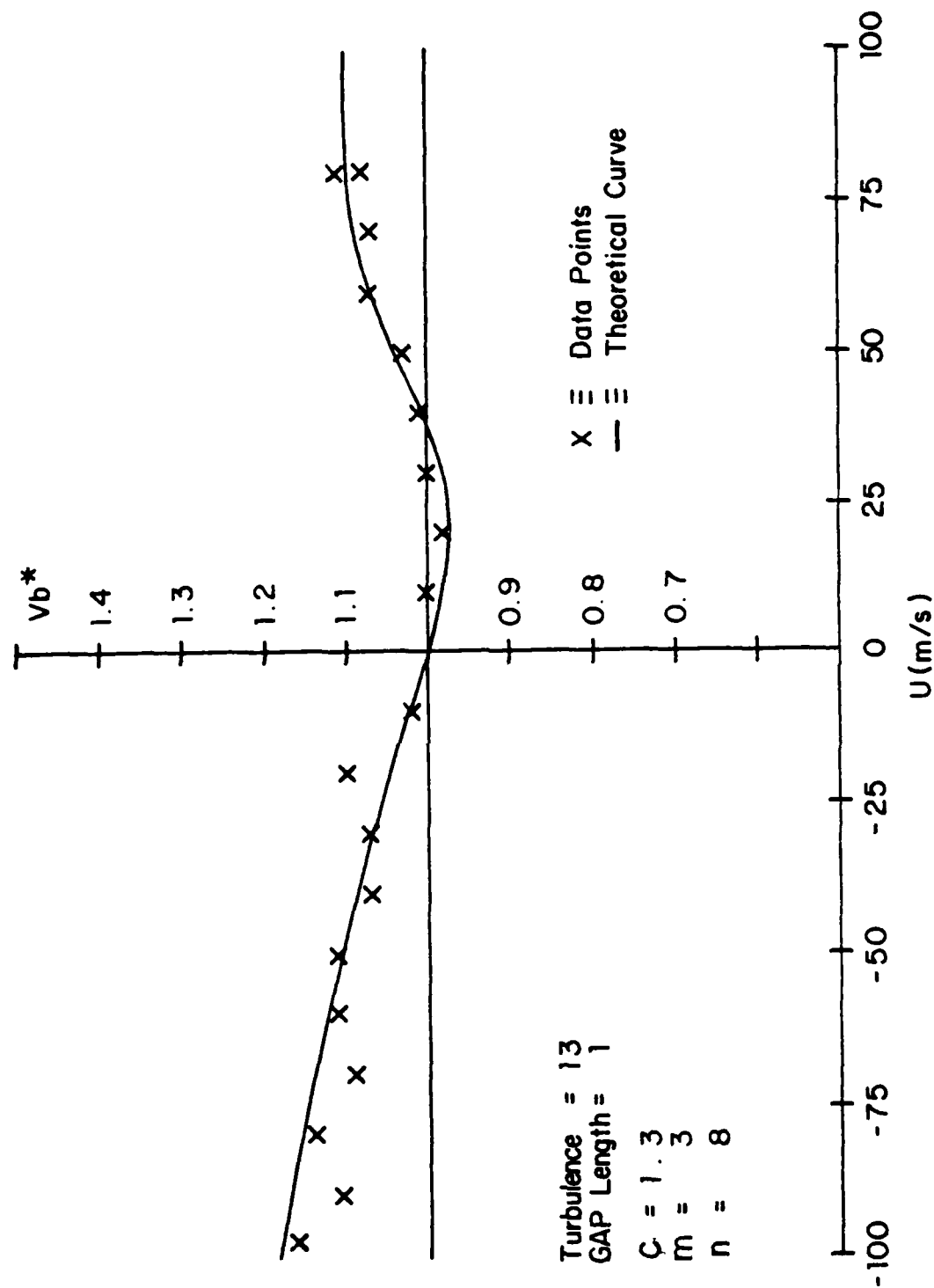
Figure 13. PLOT OF BREAKDOWN VOLTAGE VERSUS FLOW VELOCITY
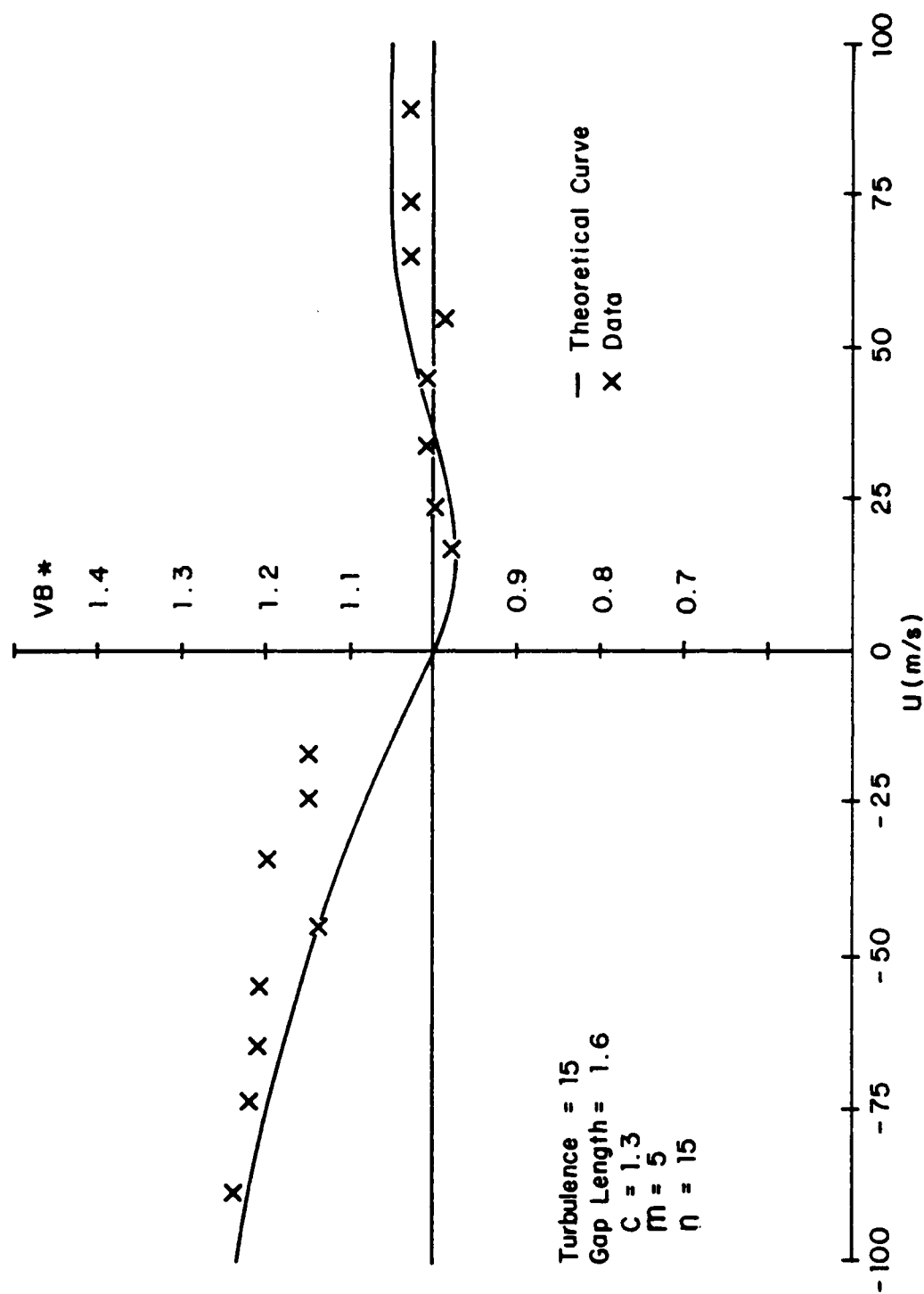
Figure 14. PLOT OF BREAKDOWN VOLTAGE VERSUS FLOW VELOCITY.
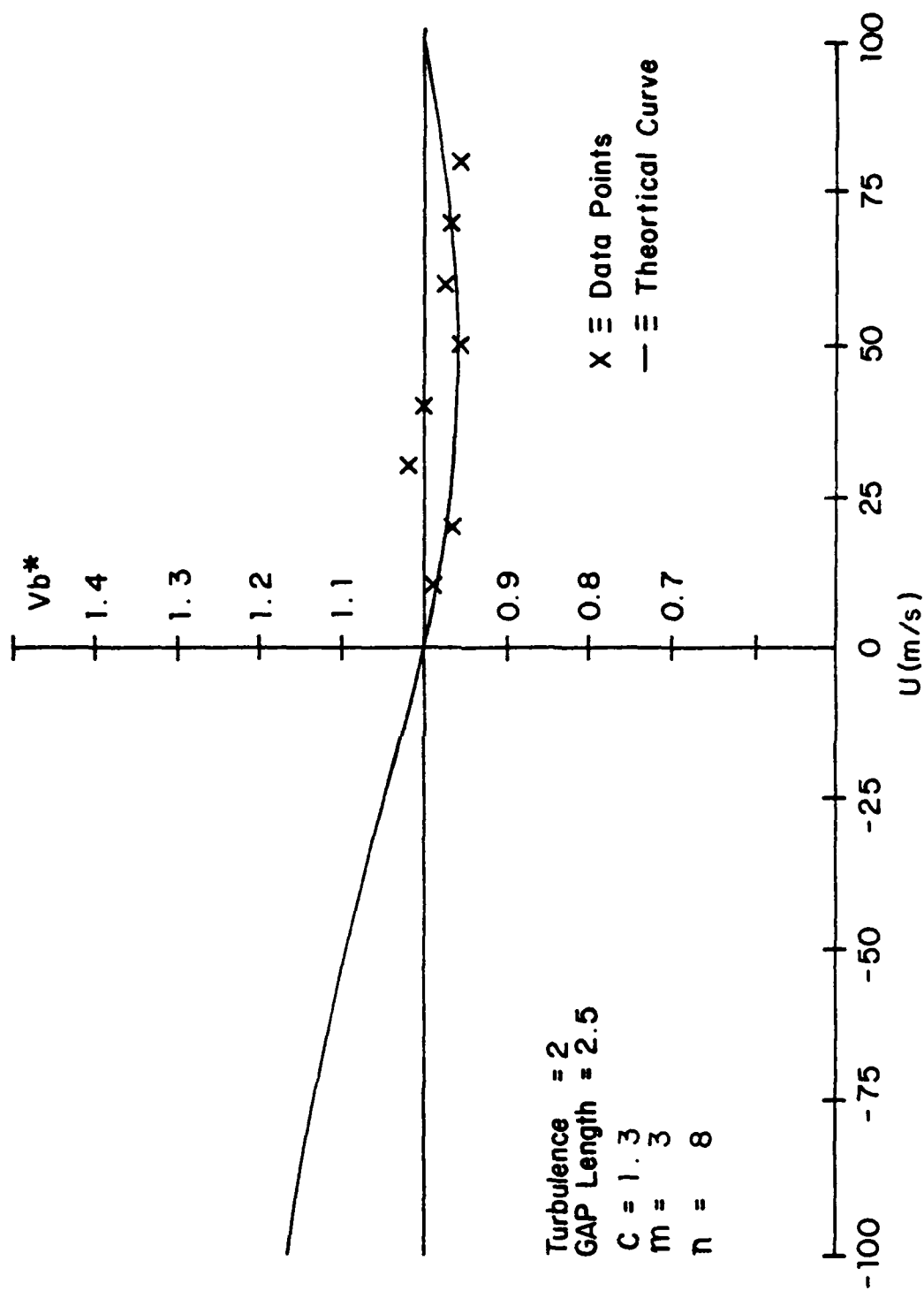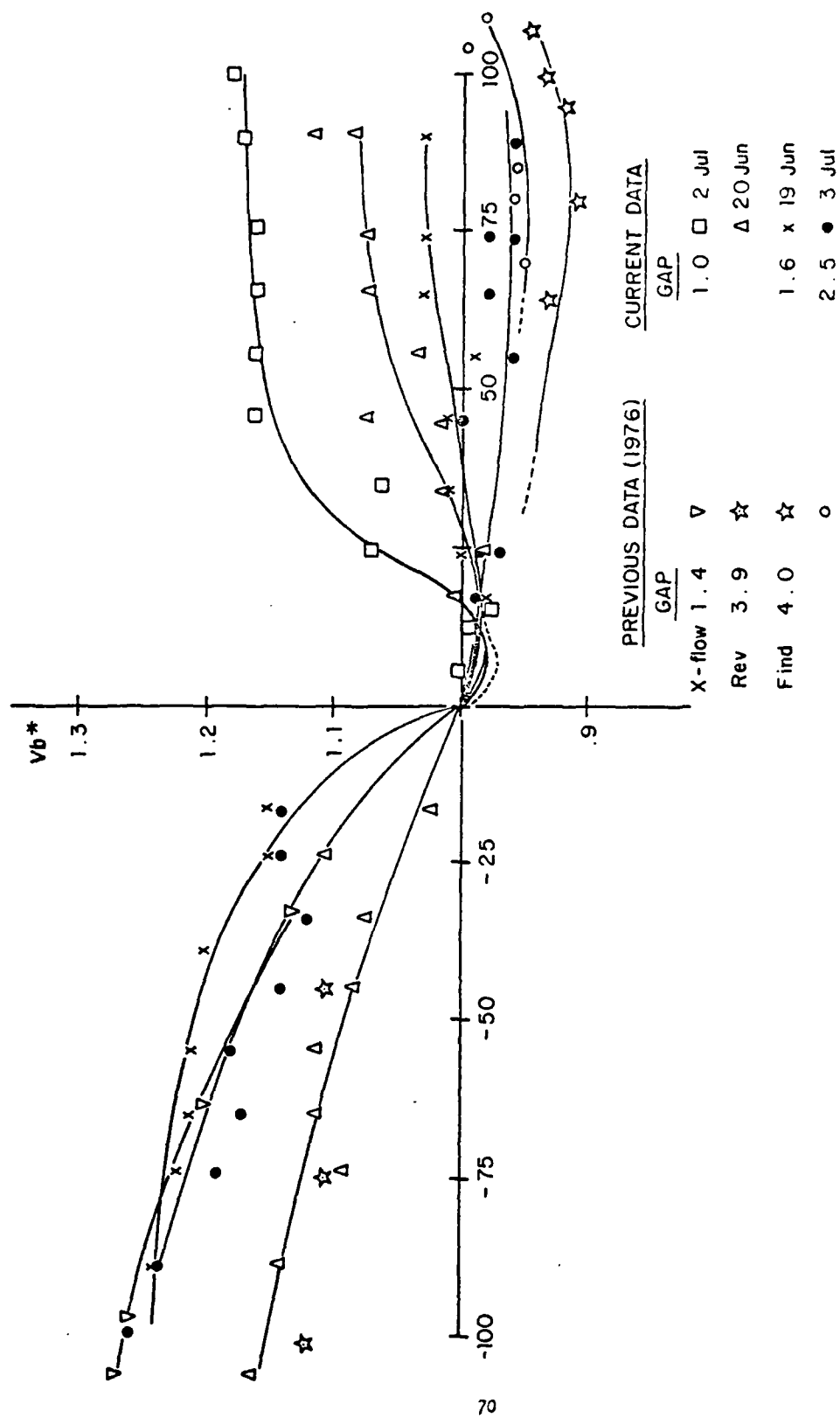
Figure 15. PLOT OF BREAKDOWN VOLTAGE VERSUS FLOW VELOCITY
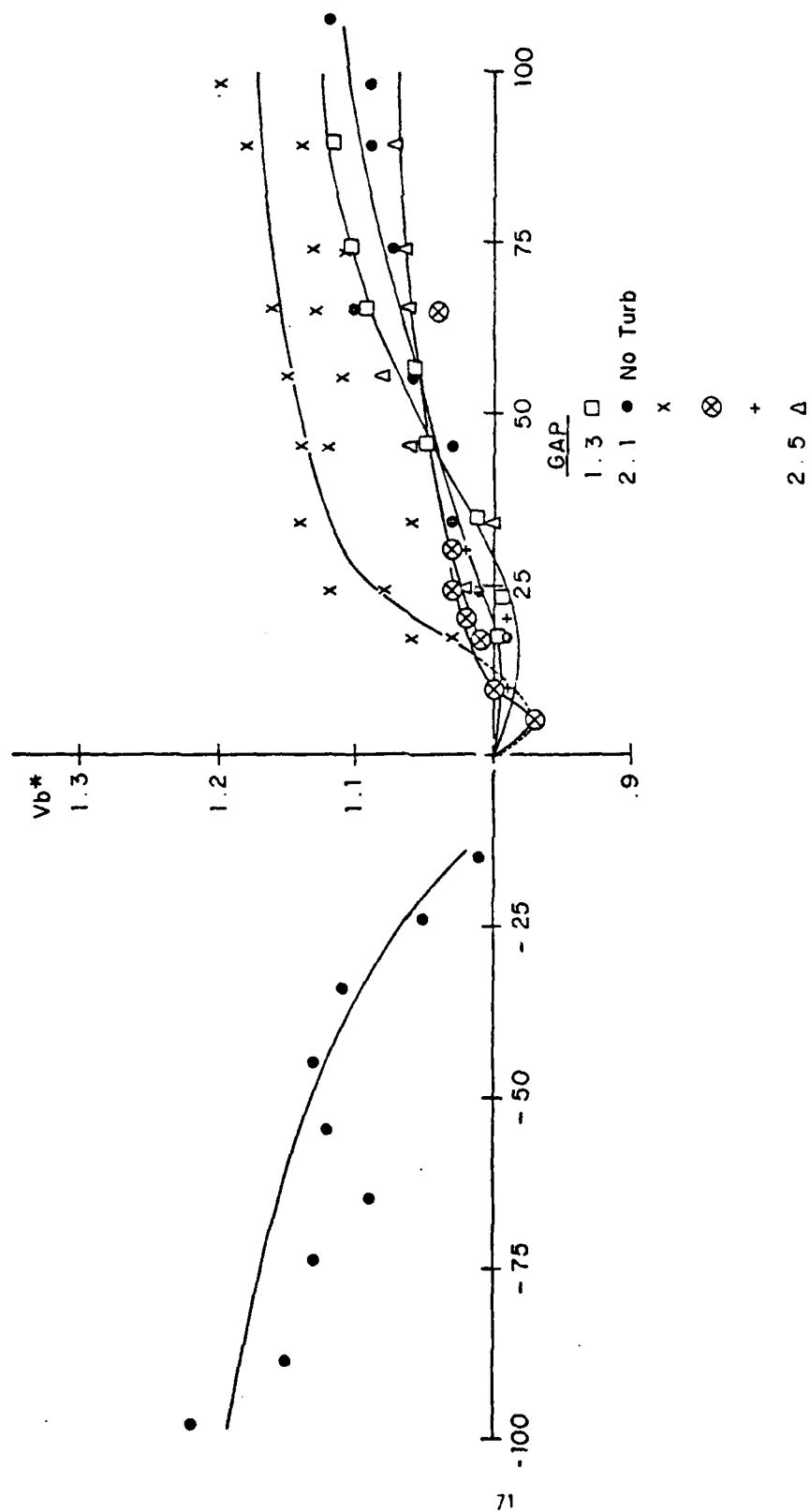
Figure 16a. POINTS TO PLANE Vb* Vs. U DATA SUMMARY.
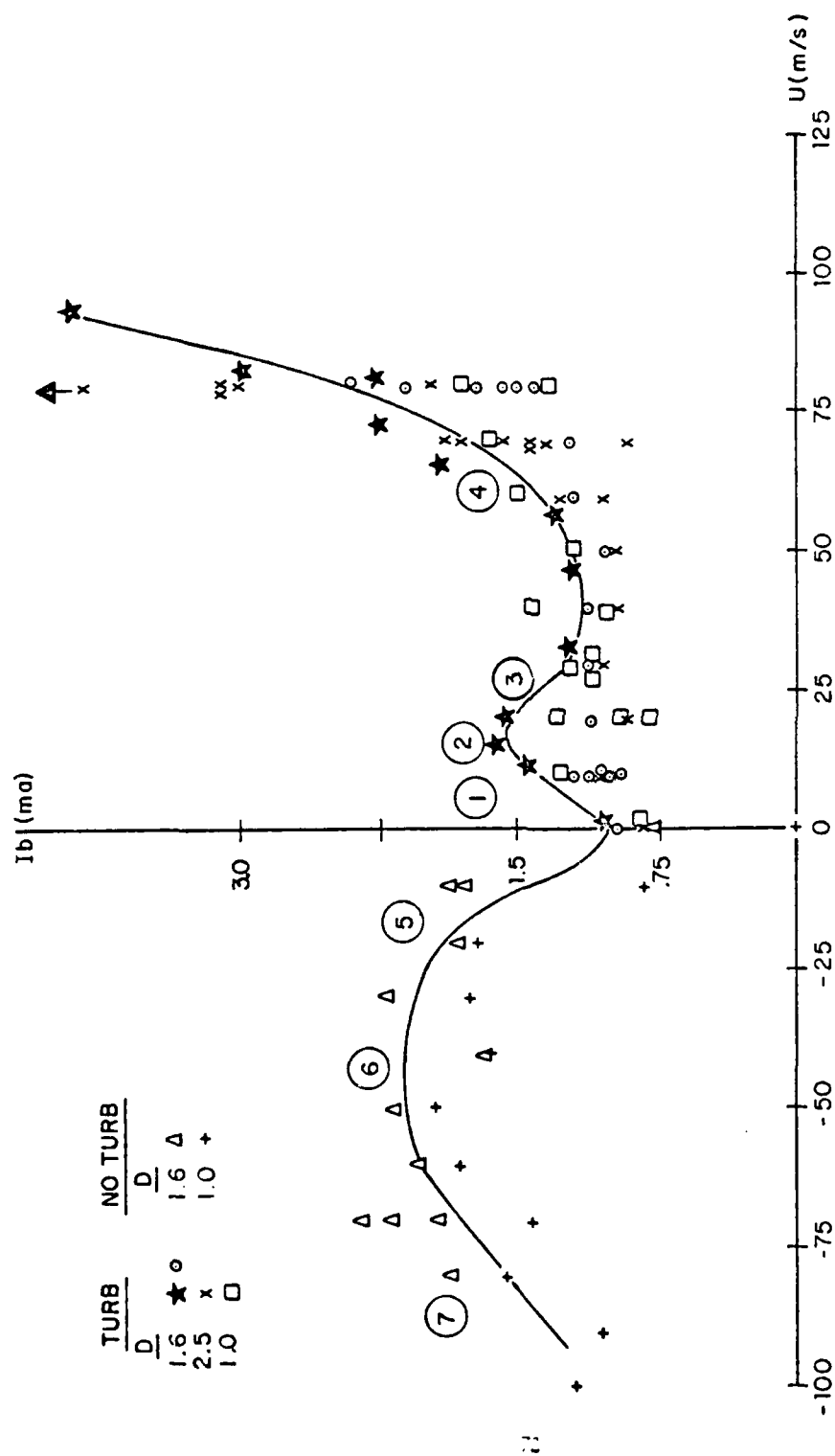
Figure 16b. WIRES–PLANE Vb* Vs. U DATA SUMMARY.

71

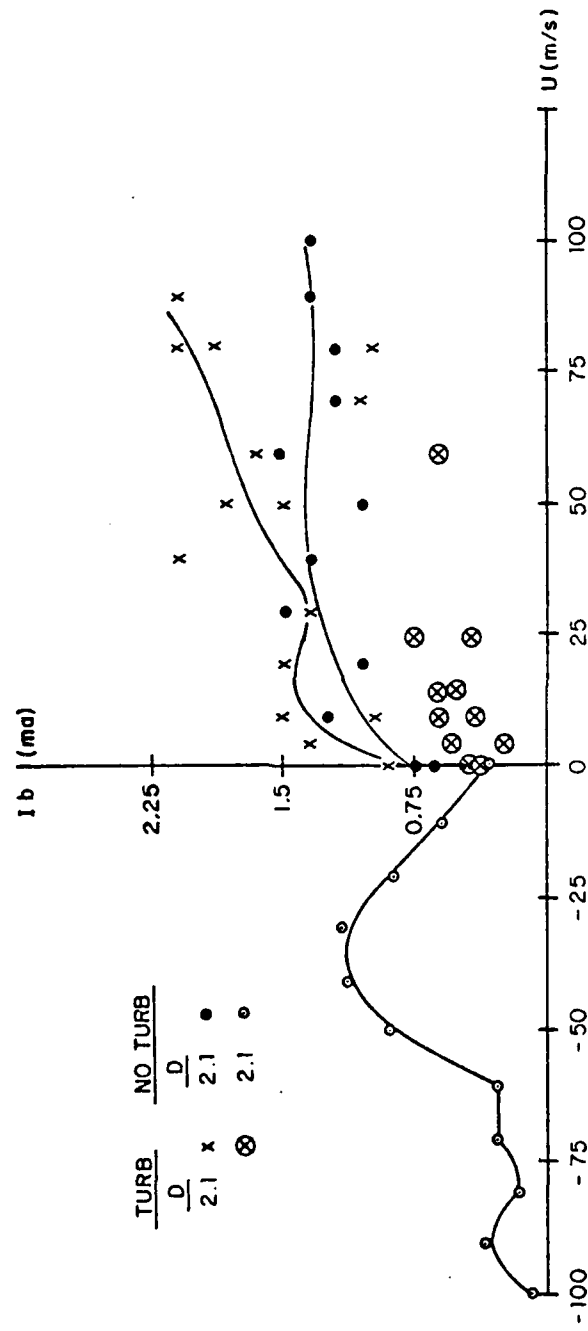Figure 17a. BREAKDOWN CURRENT Vs. FLOW VELOCITY POINT–PLANE
SUMMARY PLOT.

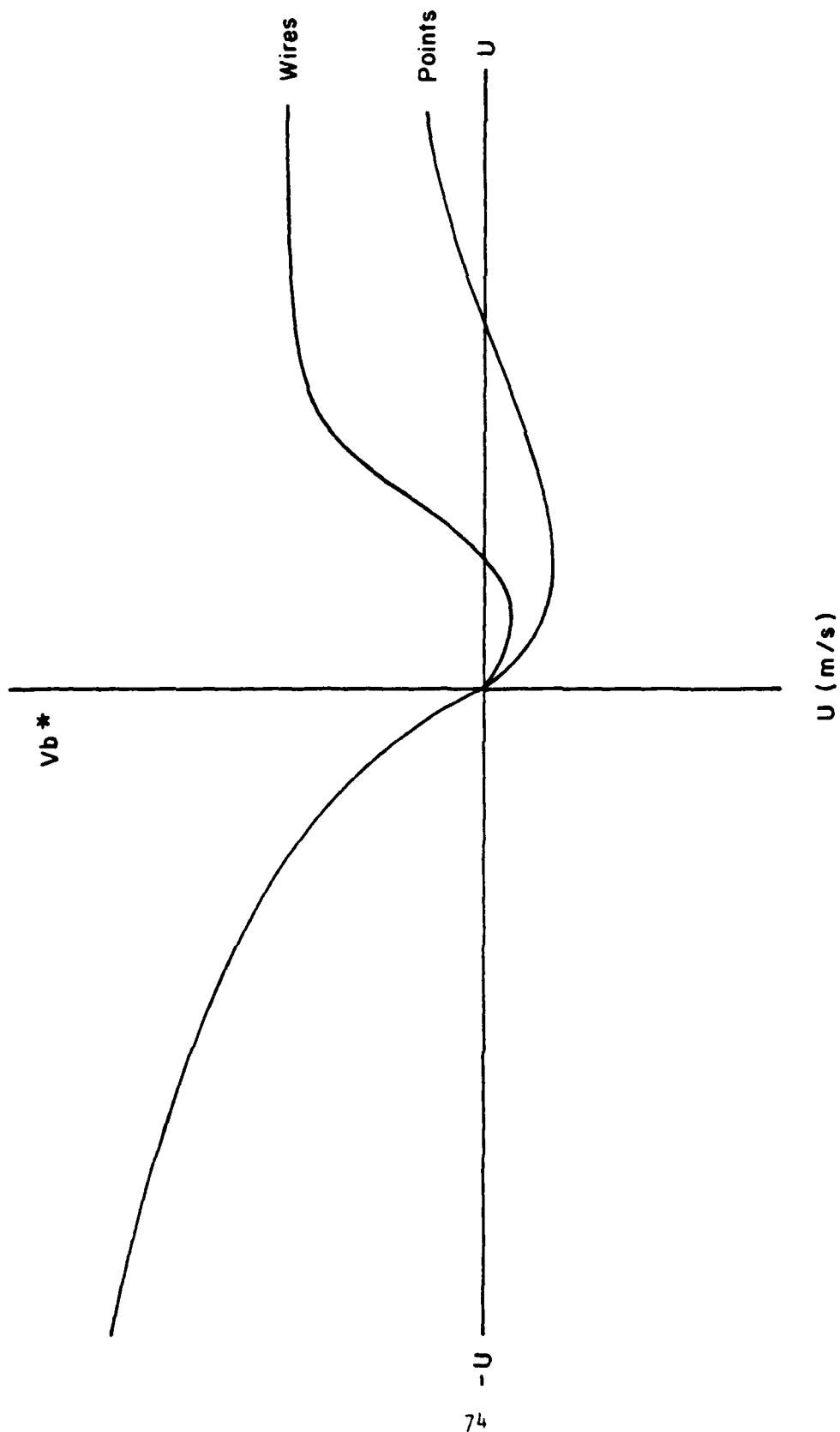Figure 17b. BREAKDOWN CURRENT Vs. FLOW VELOCITY WIRE-PLANE (3)
SUMMARY PLOT

Figure 18. TYPICAL POINT and WIRE-PLANE Vb* Vs. U DATA PATTERNS.

74

REFERENCES

1. Reilly, James P., "High Power Electric Discharge Lasers (EDL's)," American Institute of Aeronautics and Astronautics, p. 50-60, March 1975.

2. Biblarz, O. and Nelson, R. E., "Turbulence Effects on an Ambient Pressure Discharge," Journal of Applied Physics, 45, no. 2, p. 633, (February 1974).

3. Biblarz, O., Barto, J. L. and Post, H. A., "Gasdynamic Effects on Diffuse Electrical Discharges in Air", Israel J. of Tech., 15, 59 (1977).

4. Hill, A. E., "Uniform Electrical Excitation of Large Volume High Pressure Laser in Application to Laser Technology," American Institute of Aeronautics and Astronautics, Preprint No. 71-65 (1971).

5. Eckbreth, A. C., and Owen, F. S., Rev. Sci. Instrum. 43, 95̲ (1972).

6. Schwartz, Josef and Wasserstrom, E., "The Role of Gas Flow and Turbulence in Electric Discharge Lasers," Israel J. of Tech., 13, Nos. 1-2, 1975, pp. 122-133.

7. Barto, J. L., "Gasdynamic Effects on an Electric Discharge in Air," MS Thesis, Naval Postgraduate School, Monterey, CA., (Sept. 1976).

8. Meek, J. M., and Craggs, J. D., Electrical Breakdown of Gases, pp. 358-380, John Wiley and Sons, N.Y., 1978.

9. Khait, Y. and Biblarz, O., "Influence of Turbulence on a Diffuse Electrical Gasdischarge under Moderate Pressure," Journal of Applied Physics, 50, no. 7, (1979).

10. Zauderer, B. and Tate, E., "Investigation of High Power MHD Gas Lasers," Final Report AD-A013583, (August 1975).

11. Post, H. A., "Sub-ambient Controlled Turbulence Effects on Discharge Stabilization for Laser Applications," MS Thesis, U.S. Naval Postgraduate School, (Sept. 1976).

12. Nasser, Essam, Fundamentals of Gaseous Ionization and Plasma Electronics, Wiley, (1971).

13. Hirsch, M. N., and Oskam, H. J., Gaseous Electronics, pp. 222-225, Academic Press, N. Y., (1978).

14. von Engle, A., Ionized Gases, Second Edition, pp. 15-20, Oxford, (1965).

15. Raether, H., <u>Electron Avalanches and Breakdown in Gases</u>, pp. 78-84,
    Butterworths, (1964).

16. Loeb, L. B. and Meek, J. M., <u>The Mechanism of the Electric Spark</u>,
    pp. 40, 112-124, Stanford U. Press, (1941).

17. Loeb, Leonard B., <u>Electrical Coronas</u>, University of California Press,
    (1965).

18. Schlicting, H., <u>Boundary Layer Theory</u>, pp. 456-8, McGraw-Hill, (1968).

DISTRIBUTION LIST

1. Defense Technical Information Center   2
   Cameron Station
   Alexandria, Virginia 22314

2. Library   2
   Code 0212
   Naval Postgraduate School
   Monterey, California 93940

3. Office of Research Administration   2
   Code 012A
   Naval Postgraduate School
   Monterey, California 93940

4. Chairman   1
   Department of Aeronautics
   Code 67
   Naval Postgraduate School
   Monterey, California 93940

5. Professor Oscar Biblarz   5
   Department of Aeronautics
   Code 67Bi
   Naval Postgraduate School
   Monterey, California 93940

6. LCDR J. L. Barto   5
   Department of Weapon Systems Engineering
   U. S. Naval Academy
   Annapolis, Maryland 21402

7. Dr. C. Olsen, Chairman   1
   Department of Weapon Systems Engineering
   U. S. Naval Academy
   Annapolis, Maryland 21402

8. Dr. R. D. Mathieu   1
   Director of Research
   U. S. Naval Academy
   Annapolis, Maryland 21402

9. LCDR H. A. Post   1
   F-4 Weapon System Manager
   NARF NORIS
   San Diego, California 92136

10. LCDR. S. Van Brocklin   1
    Department of Aeronautics
    U. S. Naval Postgraduate School
    Monterey, California 93940

11. LT. C. Davis   1
    Department of Aeronautics
    U. S. Naval Postgraduate School
    Monterey, California 93940

12. Commander   1
    Naval Air Systems Command
    Department of the Navy
    ATTN: Dr. H. R. Rosenwasser, Code AIR 310C
    Washington, DC 20360

13. Mr. John A. Satkowski   1
    Office of Naval Research
    Power Program, Code 473
    Washington, DC 20360

14. Dr. William L. Nigham   1
    United Aircraft Research Laboratory
    East Hartford, CT 06108

15. Dr. B. N. Srivastava   1
    AVCO Everett Research Laboratory
    2385 Revere Beach Parkway
    Everett, Massachusetts 02149

16. CAPT T. A. Filcoff   1
    AFWL-AREP
    Kirtland AFB, New Mexico 87117

17. Dr. J. Shwartz   1
    TRW System
    One Space Park
    Redondo Beach, California 90278

18. Dr. Alan Garscadden   1
    AFAPL/POD
    Building 450/Room D101
    Wright-Patterson AFB, Ohio 45433

19. Dr. A. V. Phelps   1
    JILA
    Boulder, Colorado 80309